CHALMERS
UNIVERSITY OF TECHNOLOGY

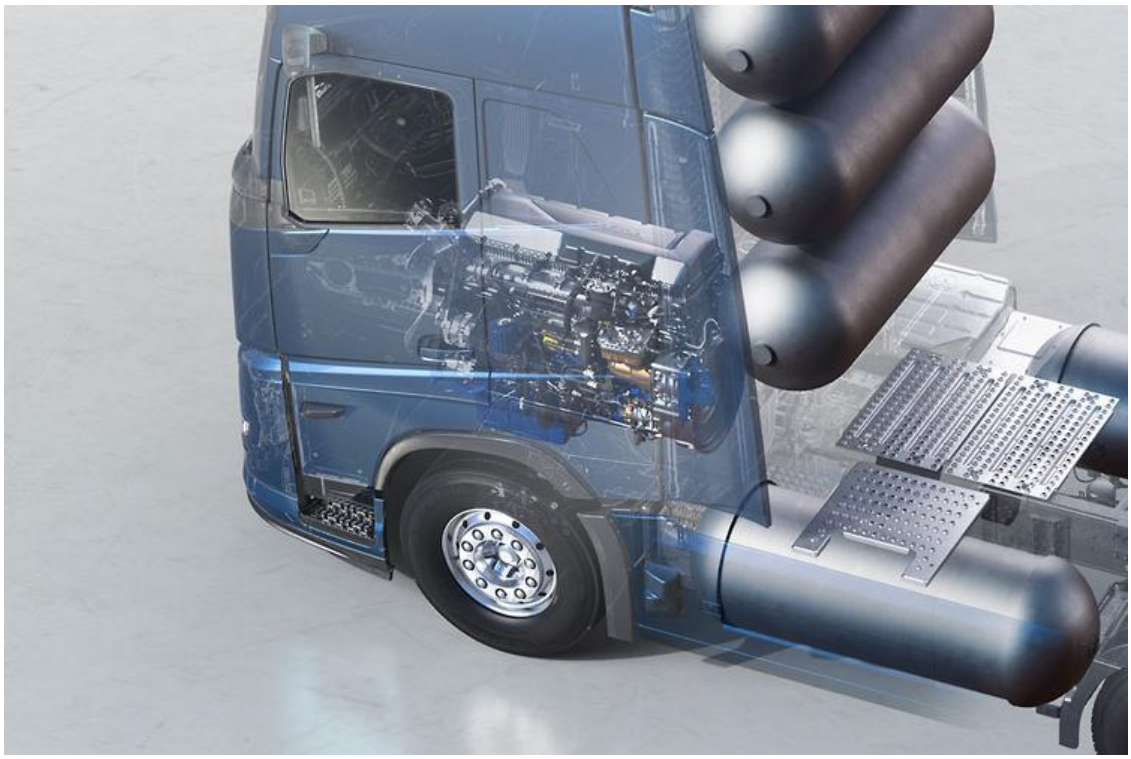

Air-path Control of a Heavy-duty Hydrogen Internal Combustion Engine

Master's thesis in Systems, Control and Mechatronics

Gideon Geelnard
Nandana Suryadevara

DEPARTMENT OF ELECTRICAL ENGINEERING

CHALMERS UNIVERSITY OF TECHNOLOGY
Gothenburg, Sweden 2025
www.chalmers.se

Master's thesis 2025

Air-path Control of a Heavy-duty Hydrogen Internal Combustion Engine

Gideon Geelnard
Nandana Suryadevara

CHALMERS
UNIVERSITY OF TECHNOLOGY

Department of Electrical Engineering
Division of Systems and Control
Chalmers University of Technology
Gothenburg, Sweden 2025

Air-path Control of a Heavy-duty Hydrogen Internal Combustion Engine
GIDEON GEELNARD
NANDANA SURYADEVARA

Supervisor: Max Edin Jakobsson, Per-Sebastian Pettersson, Volvo Technology
Examiner: Jonas Fredriksson, CTH (Division of Systems and Control)

Master's Thesis 2025
Department of Electrical Engineering
Division of Systems and Control
Chalmers University of Technology
SE-412 96 Gothenburg
Telephone +46 31 772 1000

Cover: Concept image of hydrogen powered driveline for a heavy duty truck.

Typeset in LaTeX
Printed by Chalmers Reproservice
Gothenburg, Sweden 2025

Air-path Control of a Heavy-duty Hydrogen Internal Combustion Engine
Gideon Geelnard
Nandana Suryadevara
Department of Electrical Engineering
Chalmers University of Technology

Abstract

Hydrogen internal combustion engines (H2-ICEs) offer a promising zero-carbon option to conventional diesel engines in the heavy-duty industry. This technology presents challenges in air-fuel ratio (AFR) control due to the wide flammability range and fast combustion characteristics of hydrogen. Maintaining the relative AFR (λ) value within acceptable limits is critical to reducing NO_x emissions while ensuring stable engine operation. This thesis studies the feasibility of implementing an air-path λ-control strategy to improve AFR regulation in the engine. A grey-box modeling approach was employed to map system parameters for the gas transport dynamics, utilizing engine test cell data collected under various operating conditions. The estimated parameters were then used to design and tune a feedback controller with dead time compensation. The control strategy was tested in a simulation environment, demonstrating improved λ tracking with minimal impact on the engine performance compared to a baseline strategy. The results demonstrate that air-path lambda control is a promising approach for managing the air-fuel ratio in H2-ICEs, with potential for further improvements under extended operating conditions.

Keywords: Hydrogen, Combustion, Air-path, Automotive, Sensor fusion, Dynamic systems, Embedded control, Simulation.

Acknowledgements

First, we would like to thank our supervisors at Volvo Technology, Max Edin Jakobsson and Per-Sebastian Pettersson, for their continued support throughout this project. Their extensive knowledge of combustion theory and ICE systems have been invaluable to the achievement of this thesis.

Next, we would like to extend our gratitude to Professor Jonas Fredriksson, our supervisor and examiner. His advice on control theory and system identification was proven to be imperative for overcoming obstacles.

We are also grateful to Matilda Törngren, our group manager, for making this thesis a possibility. Thank you.

For all the support and guidance related to the simulation environment and for enhancing our understanding of engines, we would like to thank Carl Sjöstedt. Also, thanks for the ride along in the truck.

Additionally, we extend our thanks to the entire Combustion System Control team at Volvo Technology for welcoming us into the team.

Lastly, we would like to thank our families for their love and support.

Gideon Geelnard, Gothenburg, June 2025
Nandana Suryadevara, Gothenburg, June 2025

List of Acronyms

Below is the list of acronyms that have been used throughout this thesis listed in alphabetical order:

AFR	Air-to-Fuel Ratio
CVI	Constraint Violation Integral
DI	Direct Injection
EGR	Exhaust Gas Recirculation
FOPDT	First-Order Plus Dead Time
H2-ICE	Hydrogen Internal Combustion Engine
ICE	Internal Combustion Engine
ITV	Intake Throttle Valve
PID	Proportional-Integral-Derivative
QP	Quadratic Programming
RMSE	Root Mean Square Error
RPM	Revolutions Per Minute
SQP	Sequential Quadratic Programming
VGT	Variable Geometry Turbo

Nomenclature

Below is the nomenclature of indices, transfer functions, sets, parameters, and variables that have been used throughout this thesis.

Indices

i	Index for Padé approximation coefficients
j	Index for data points in kernel smoothing
k	Iteration index for SQP
k_p	Index for differentiation order in Padé approximation
k_s	Iteration index for Simulated Annealing

Transfer Functions

$\bar{F}$	Transfer function of controller
F	Transfer function of controller with an Otto-Smith predictor
$\bar{G}$	Transfer function of the plant without dead time
G	Transfer function of the plant including dead time
G_n	Padé approximation of the time delay
G_{ry}	Closed-loop system transfer function
H	Transfer function of noise model
L	Open-loop system transfer function
S	Sensitivity function of the system

Sets

$\mathbf{Z}^N$	Set of input-output data for system identification

Parameters

AFR_{stoic}	Stoichiometric air-to-fuel ratio
$AFR_{stoic,diesel}$	Stoichiometric air-to-fuel ratio for diesel
AFR_{stoic,H_2}	Stoichiometric air-to-fuel ratio hydrogen
f	Objective function for Simulated Annealing
M_s	Maximum sensitivity of the system
$M_{s,\max}$	Maximum allowed maximum sensitivity of the system
n_p	Order of the Padé approximation
N	Number of samples used for system identification
R	Ideal gas constant $[J/(mol \cdot K)]$
tol	Tolerance for solution produced by the Simulated Annealing algorithm
V_N	Cost function for system identification
$\mathcal{L}$	Lagrangian function for the constrained optimization
α_p, β_p	Padé approximation coefficients
α_t	Cooling rate in the Simulated Annealing algorithm
β	Tuning parameter for the PID controller
λ_{max}	Maximum allowed relative air-to-fuel ratio
λ_{min}	Minimum allowed relative air-to-fuel ratio
λ_{target}	Target relative air-to-fuel ratio
ϕ	Merit function used in line search
ζ	PID damping ratio
θ	Parameter vector for system identification
$\theta_{\max}$	Upper bound for parameter vector in SQP
$\theta_{\min}$	Lower bound for parameter vector in SQP

Variables

AFR_{actual}	Current air-to-fuel ratio
b	Fraction of burned air in the intake manifold
CVI_{lc}	Integral outside the lambda-limits using lambda control $[\lambda s]$
CVI_r	Integral outside the lambda-limits using baseline control $[\lambda s]$

CVI_{woOS}	Integral outside the lambda-limits without using Otto-Smith compensator [λs]
c_1, c_2	Coefficients for discrete low-pass filter
d	System delay term in the Z-domain
f_{tol}	Function tolerance for SQP
K	Static gain of the process
K_d	Derivative controller gain
K_i	Integral controller gain
K_p	Proportional controller gain
L	Gas transport delay [s]
M	Molar mass of gas [g/mol]
m_{air}	Air mass [g]
m_{fuel}	Fuel mass [g]
$m_{fuel,lc}$	Fuel mass consumed using lambda control [kg]
$m_{fuel,r}$	Fuel mass consumed using baseline control [kg]
n	Number of moles of gas [mol]
P	Pressure [kPa]
P_a	Acceptance probability of a worse solution in Simulated Annealing
p_e	Exhaust manifold pressure [kPa]
p_i	Intake manifold boost pressure [kPa]
p_{req}	Requested boost pressure [kPa]
$RMSE_{\lambda,lc}$	Root Mean Square Error value for lambda using lambda control
$RMSE_{\lambda,r}$	Root Mean Square Error value for lambda using baseline control
$RMSE_{\lambda,woOS}$	Root Mean Square Error value for lambda without using the Otto-Smith compensator
$RMSE_{\text{torque},lc}$	Root Mean Square Error value for torque using lambda control [Nm]
$RMSE_{\text{torque},r}$	Root Mean Square Error value for torque using baseline control [Nm]
$RMSE_{\text{torque},r}$	Root Mean Square Error value for torque without using the Otto-Smith compensator[Nm]
R	Ideal gas constant [8.314 J/(mol·K)]
s_{tol}	Step tolerance for SQP
T	Temperature [K]
T_d	Derivative PID time constant [s]
T_f	Low-pass filter time constant for derivative PID term [s]

T_i	Integral PID time constant $[s]$
T_{in}	Intake manifold boost temperature [K]
$T_{in,req}$	Intake manifold boost temperature corresponding to requested air mass flow [K]
T_s	Sampling period $[s]$
T_{SA}	Temperature in the Simulated Annealing algorithm
u	Input signal to the system
V	Volume [m^3]
v	Constraint violation metric
y	Measured output signal of the system
ΔE	Increase in the objective function value between current and candidate solution in Simulated Annealing
e_λ	Error between measured and requested lambda
e_p	Prediction error between measured output and model output
λ	Relative air-to-fuel ratio
λ_{feas}	Feasible relative air-to-fuel ratio to input to engine cylinders
λ_{in}	Calculated relative air-to-fuel ratio input to the engine cylinders
λ_{meas}	Measured relative air-to-fuel ratio
$\lambda_{\mathcal{L}}, \mu_{\mathcal{L}}$	Lagrange multipliers associated with inequality constraints in SQP
$\mathcal{P}$	Poles of closed loop system
ρ	Penalty parameter in merit function for SQP
σ	Kernel width in Gaussian Smoothing
σ_A	Armijo parameter for line search
σ_{param}	Kernel width in Gaussian Smoothing of system parameter map
σ_{PID}	Kernel width in Gaussian Smoothing of PID constants map
σ_{prep}	Kernel width in Gaussian Smoothing for data preprocessing
τ	Controller time constant $[s]$
τ_g	Gas dynamics time constant [s]
ω_c	Low-pass filter cutoff frequency [rad/s]
$\mathcal{Z}$	Zeros of closed loop system

Contents

List of Figures

List of Tables

1

Introduction

Initiatives for reducing emissions and protecting the environment are increasing due to the global demands set by the Paris Agreement, which is a multilateral treaty. The treaty legally binds all signed nations to uphold the set commitments, which include the goal of net-zero emissions [1]. These initiatives have driven the technological development of alternative energy sources for vehicles, particularly for heavy-duty trucks. One such solution is the hydrogen internal combustion engine (H2-ICE), which replaces fossil-based fuels used in traditional internal combustion engines (ICEs) by using fossil-free fuel. Without hydrocarbons in the fuel, the primary emission for H2-ICEs is water vapor [2]. H2-ICE technology offers solutions to the challenges faced by its electric counterpart [3], such as long charging times and limited range. Hydrogen technology is favorable for long distances, offers shorter charging times, and minimizes dependence on rare-earth materials. With the development of new engine technology, new challenges arise in combustion control. New control strategies for the air-fuel ratio (AFR) are necessary to achieve optimality for hydrogen combustion. It is imperative that the efficiency of the practical implementation is equivalent to that of the existing solution to make it a commercial reality.

1.1 Purpose

The purpose of this thesis is to develop an airflow-based control strategy using λ sensor feedback. The solution strategy is aimed at hydrogen combustion in heavy-duty vehicles, contributing to the development of carbon-free technology. The resulting control strategy is developed to optimize the efficiency of H2-ICEs, investigating the possibilities and limits of hydrogen combustion. The implementation of the control strategy is evaluated by assessing how well it manages the air-path system to achieve a target AFR. A prototype model is used for validation, created from the existing framework for the diesel ICE. The goal of the control strategy is to ensure that the λ-value is kept within the optimal range for hydrogen combustion, considering both exhaust emissions and vehicle performance. An additional objective of the control strategy is adaptivity to varying dynamics, for example, transient conditions. The results of this thesis contribute to the development of efficient H2-ICE, addressing challenges associated with λ-control for hydrogen combustion.

1.2 Problem Statement

The primary objective of this thesis is to develop a strategy for λ-control in H2-ICEs, utilizing an existing framework for diesel internal combustion engines. This is achieved through the development of parameter maps for gas exchange and transport dynamics, the design of air-path control strategies for effective lambda regulation, and the evaluation of their impact on engine performance and drivability.

1.3 Ethical Aspects

The primary ethical aspect under consideration, with regard to this thesis, is the environmental impact. Hydrogen technology is an alternative energy source for heavy-duty vehicles that operate long distances with heavy loads. This alternative provides an opportunity for the automotive industry to transition to greener solutions. Another important consideration for utilizing hydrogen technology is the production of hydrogen. The production of hydrogen can be achieved through various processes, some of which are not green. The use of hydrogen technology is considered green solely when the production of said hydrogen is also green. The European Commission promotes the development of clean hydrogen technology through an alliance established in 2020 [4].

Other aspects to consider when developing hydrogen technology are health and safety. Primary concerns with hydrogen management are storage and flammability. Hydrogen storage challenges arise from the need for compatible metals in hydrogen tanks and the low storage capacity of hydrogen due to its low density [5]. Hydrogen is highly flammable, increasing the importance of identifying possible ignition sources and conditions. Possible hydrogen gas leaks pose a flammable risk and have negative health and environmental impacts [5]. Using hydrogen in large-scale operations requires safety regulations to ensure public health and safety. It is essential to conduct risk assessments for potential hazards and contingencies. Such assessments should be unique to each use case and regularly updated to ensure that emergency procedures are up-to-date.

1.4 Limitations

This thesis focuses on developing a control strategy that translates the measured lambda value into a corresponding boost pressure request. An existing control strategy determines the execution of the boost pressure request; no alterations are implemented. The developed control strategy is implemented in the existing diesel framework and tested in the corresponding simulation environment. Because the emission data is based on a diesel engine and does not accurately reflect the emission profile of hydrogen combustion, the performance evaluation is limited to the ability to track lambda. Finally, the EGR dynamics are not considered for the design of the control strategy.

1.5 Thesis Outline

Chapter 2, following the Introduction, presents relevant theory for understanding combustion, engine air-path, system modeling, control theory, and parameter identification. Chapter 3 presents the methods for implementing the proposed lambda control strategy. The results are presented in Chapter 4 and discussed in Chapter 5.

2
Theory

This chapter outlines the theoretical background for the project. It covers the basic operation of internal combustion engines, key concepts of control theory, performance metrics for determining the effectiveness of a control strategy, and techniques for parameter identification and mapping.

2.1 Combustion Theory and Engine Air-path

This section covers the relevant theory for understanding the combustion process in an internal combustion engine (ICE).

2.1.1 ICE Fundamentals

Combustion engines extract energy from the injected fuel by converting chemical energy into mechanical power. The basic principle of a combustion engine is that oxygen reacts with fuel to release the stored chemical energy. The combustion occurs inside a cylinder, causing movement to the piston as depicted in Figure 2.1. The motion transfers mechanical power to a crankshaft via a connecting rod.

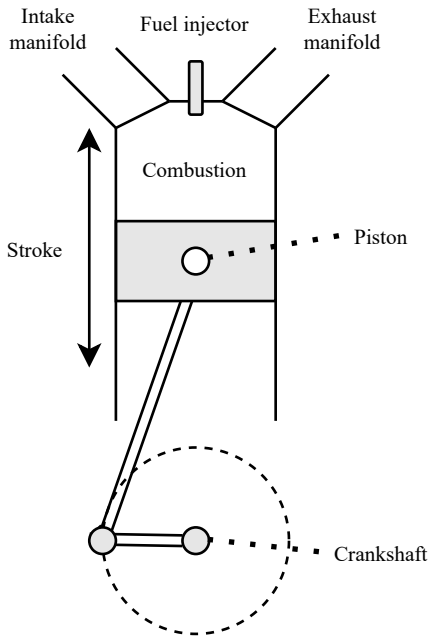

Figure 2.1: Internal geometry of a four-stroke direct injection (DI) engine.

In this thesis, the engine is a four-stroke direct injection ICE. As the name suggests, a four-stroke engine has an operating cycle consisting of four distinct stages: intake, compression, expansion, and exhaust. During the intake stroke, the intake manifold valve opens, allowing air into the combustion chamber as the piston is pushed to the bottom of the cylinder. Next in the compression stroke, both valves close as the piston moves toward the top, compressing the air within the cylinder. After the air is compressed, fuel is injected into the combustion chamber through the fuel injector. Ignition occurs during the start of the expansion stroke, as the piston reaches its top position. As the air-fuel mixture combusts, thermal energy is released. The expansion from the combustion forces the piston down to the bottom, generating five times the work of the piston during the compression stroke. Lastly, during the exhaust stroke, the exhaust manifold valve opens. This allows the gases from the combustion chamber to exit, completing one cycle of the four-stroke engine, [6].

2.1.2 Stoichiometric Combustion

The air-fuel ratio (AFR), defined as the ratio between the amounts of air, m_{air}, and fuel, m_{fuel}

$$\text{AFR} = \frac{m_{air}}{m_{fuel}} \tag{2.1}$$

is crucial for the efficiency of the combustion process. A certain amount of oxygen in the air-fuel mixture will cause the injected fuel to completely combust. The optimal ratio is defined as the stoichiometric AFR and is crucial for the composition of the exhaust gases. The ratio between the actual AFR and the optimal AFR, AFR_{actual}, is denoted as λ, and is calculated as

$$\lambda = \frac{\text{AFR}_{actual}}{\text{AFR}_{stoic}}. \tag{2.2}$$

Air-fuel mixtures outside stoichiometric conditions are described as fuel-rich or fuel-lean. In conditions where the amount of oxygen is less than optimal, the AFR is classified as fuel-rich. The AFR is considered fuel-lean when the amount of fuel is less than the stoichiometric value [6]. Using (2.2), $\lambda = 1$ for stoichiometric mixtures, $\lambda > 1$ for fuel-lean, and $\lambda < 1$ for fuel-rich.

2.1.3 Combustion Chemistry

The ideal combustion process disregards the nitrogen in the air, which in reality affects the composition of the exhaust gases. An example of combustion for diesel is [7]

$$4\text{C}_{12}\text{H}_{23} + 71\text{O}_2 \rightarrow 48\text{CO}_2 + 46\text{H}_2\text{O}. \tag{2.3}$$

In ideal combustion, all fuel is oxidized and the by-products are CO_2 (carbon dioxide) and H_2O (water). For diesel, the stoichiometric ratio, [6], is

$$AFR_{stoic,diesel} = 14.5. \tag{2.4}$$

Despite ideal conditions, diesel combustion has been proven to have a negative impact on the climate. The release of CO_2 negatively impacts the environment by contributing to the increase in atmospheric temperature [8].

Considering ideal combustion for a hydrogen engine instead, the following reaction takes place:

$$2H_2 + O_2 \rightarrow 2H_2O. \tag{2.5}$$

The only by-product of ideal hydrogen combustion is H_2O (water) [2]. From the reactions presented in (2.5) [6] and (2.3), it can be observed that nitrogen is not involved in ideal combustion. The stoichiometric AFR for hydrogen combustion according to [6] is

$$AFR_{stoic,H_2} = 34.3. \tag{2.6}$$

In contrast to the ideal condition, nitrogen in the air tends to react with oxygen during the combustion process, forming nitrogen oxide (NO_x) emissions. These emissions form at high temperatures and pressures during the combustion process [6]. To counteract the formation of NO_x emissions, the conditions within the combustion chamber need to be controlled. The formation of NO_x, for hydrogen combustion engines, is close to zero with a $\lambda > 2$ [9]. Active λ-control is therefore required to regulate the NO_x emissions during operations to a negligible value. However, this must be done without negatively impacting the engine's performance. For example, if the mixture is too fuel-lean, it can lead to engine misfire and loss of performance [6]. During transient conditions, the λ should be allowed to deviate in order not to sacrifice engine power. Additionally, the mixture cannot become too rich, as this would lead to engine knocking, which occurs when the autoignition of the air-fuel mixture takes place. Ideally, the relative AFR would be somewhere in the range $1.8 < \lambda < 2.7$ [10]. This range might vary depending on the engine.

2.1.4 Engine Air-path

This section covers the various components that comprise the engine air path, as well as the relevant sensors and actuators used in this thesis. The theory presented in this section is based on [6]. Figure 2.2 shows a simplified flow chart of the engine air-path.

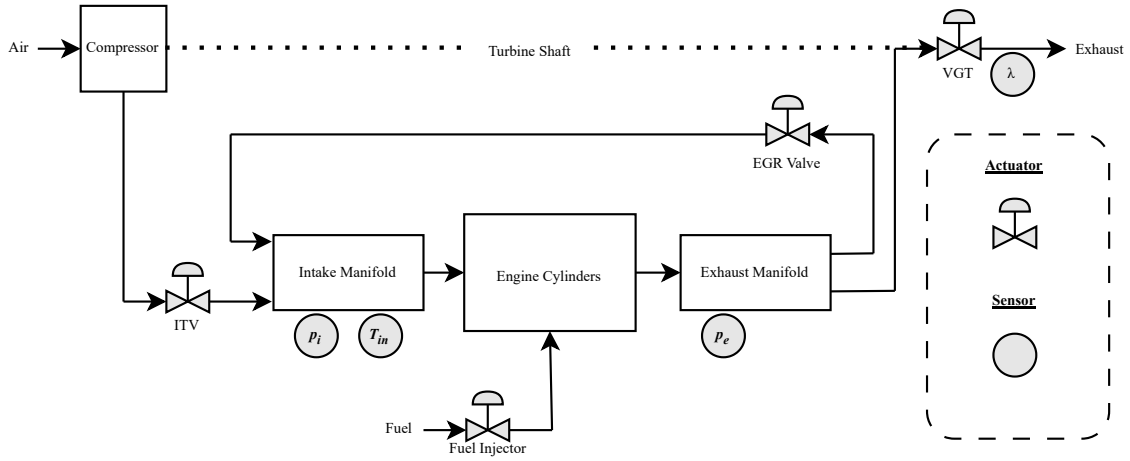

Figure 2.2: Simplified engine air-path.

The air path begins at the compressor, where ambient air is drawn in. The speed of the compressor can be finely tuned using a variable geometry turbocharger (VGT). The VGT's ability to adjust its internal geometry allows it to modulate the speed of the turbine shaft, thereby influencing the airflow entering the compressor. The VGT can effectively control the boost pressure generated by the turbocharger. However, the VGT's response time can be slow, particularly during certain transient behaviors. After the compressor, the air is cooled and directed to the intake throttle valve (ITV). By adjusting the throttle position, the system can effectively control the volume of air entering the intake manifold. The VGT generates the boost pressure, establishing an upper limit on air mass that can flow into the intake manifold. This is where the ITV provides a more precise means of regulating the air mass flow into the engine intake. By allowing for rapid adjustments, the ITV can enhance the overall responsiveness of the engine, resulting in good performance under varying driving conditions.

The intake manifold precedes the combustion chamber, as seen in Figure 2.2. In this DI engine, it is responsible for distributing air and exhaust gases to the engine cylinders. Inside the manifold, two sensors are located to monitor the intake manifold pressure (p_i) and temperature (T_{in}). It is assumed that the control structure between the boost pressure demand and the adjustment of the VGT and ITV has been established. Consequently, boost pressure is treated as a direct control input to the air-path controller, rather than tracing the entire process back through the VGT geometry.

In a DI engine, fuel is injected directly into the combustion chamber. The fuel injector distributes the fuel under high pressure to the engine cylinders. This is done to achieve an even distribution of gaseous hydrogen, which enhances flame propagation speed and combustion efficiency. The fuel injector enables precise control over the injected fuel, eliminating uncertainties common in port-injection engines, such as fuel film buildup. The combustion processes, where the chemical energy of the fuel is extracted, occur in the engine cylinders as previously mentioned in Section 2.1.1.

With control of the fuel injectors and air distribution in the intake manifold, the AFR can be accurately controlled.

After combustion, the exhaust gases are ejected out of the cylinder and into the exhaust manifold, where a pressure sensor detects the exhaust pressure (p_e). Exhaust gases are distributed (through the VGT) to the exhaust system where λ is measured, alternatively to the EGR valve. One effective method for reducing the temperatures of the engine cylinders is the use of exhaust gas recirculation (EGR) controlled by the EGR valve. As discussed in Section 2.1.3, the formation of NO_x occurs at higher combustion temperatures. At part load, the EGR helps to dilute the air-fuel mixture, which lowers the combustion temperature. The exhaust gases from the EGR, mainly composed of water vapor, increase the thermal capacity of the air-fuel mixture. Consequently, the exhaust gases will act as inert gases during the combustion process.

2.2 Control Theory

This section covers the relevant theory for the control strategy and the subsequent stability analysis.

2.2.1 PID Controller

A proportional-integral-derivative (PID) controller is based on a control loop algorithm that continuously calculates an error value as the difference between a desired set-point and the measured process variable. The controller applies a correction based on three terms: proportional (P), integral (I), and derivative (D), each contributing to the overall control action. The parallel form of a PID controller can be expressed as a transfer function [11]:

$$\bar{F}(s) = K_p + \frac{K_i}{s} + K_d s. \tag{2.7}$$

The proportional term, with gain K_p, generates an output proportional to the current error, thereby improving response speed but potentially leaving a steady-state error. The integral term, weighted by K_i, accumulates past errors to eliminate steady-state error. However, if K_i is too large, it can cause an overshoot and oscillations. The derivative term scaled by K_d considers the rate of change of the error to improve stability and reduce overshoots.
The derivative term can be expressed in the low-pass filter form [11], rewriting the transfer function as

$$\bar{F}(s) = K_p \left(1 + \frac{1}{T_i s} + \frac{T_d s}{1 + T_f s}\right). \tag{2.8}$$

The PID controller expressed in general form is

$$\bar{F}(s) = K_i \frac{1 + 2\zeta s\tau + (s\tau)^2}{s(1 + s\tau/\beta)} \tag{2.9}$$

where:

$$2\zeta\tau = T_i + T_f \tag{2.10}$$
$$\tau^2 = T_i(T_d + T_f) \tag{2.11}$$
$$\beta = \frac{\tau}{T_f} \tag{2.12}$$

and the controller gains for tuning are

$$K_i = \frac{K_p}{T_i} \tag{2.13}$$
$$K_d = K_p T_d. \tag{2.14}$$

2.2.2 Otto-Smith Predictor

When dead time is present in the plant model, predictive action in the control loop is required to avoid instabilities. Methods that are computationally heavy, such as model predictive control using a receding horizon, are rejected due to the engine's too fast dynamics. The Otto-Smith predictor is a more feasible approach for systems with significant dead time [12].

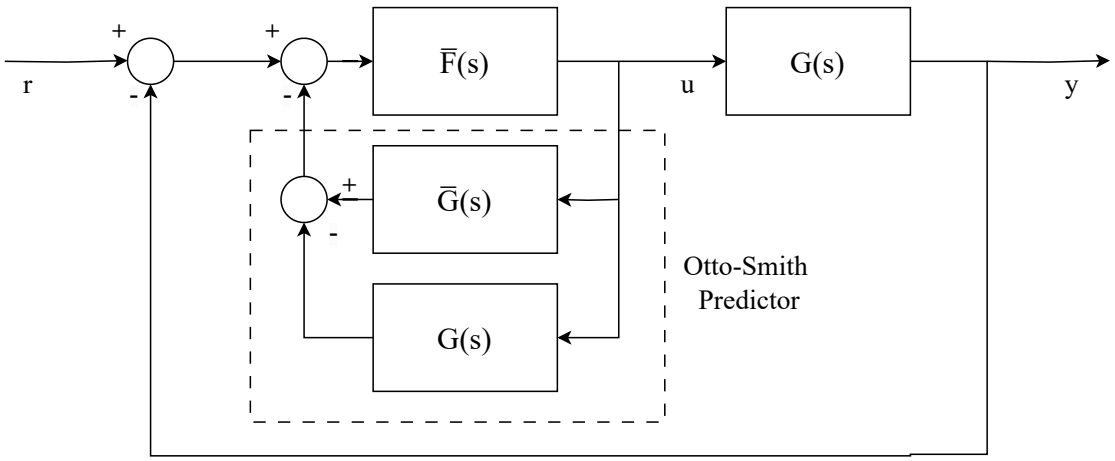

Figure 2.3: Otto-Smith predictor in the closed loop system.

The Otto-Smith predictor is constructed as shown in Figure 2.3, and the corresponding transfer function is [13]:

$$F(s) = \frac{\bar{F}(s)}{1 + (1 - e^{-sL})\bar{G}(s)\bar{F}(s)} \tag{2.15}$$

where $\bar{F}(s)$ is the controller transfer function without the added Otto-Smith predictor and $\bar{G}(s)$ is the plant model without the dead time. The open-loop form for the transfer function is denoted as $L(s)$ [11], written as

$$L(s) = G(s)F(s) = \frac{\bar{G}(s)\bar{F}(s)e^{-sL}}{1 + (1 - e^{-sL})\bar{G}(s)\bar{F}(s)}. \tag{2.16}$$

2.2.3 Stability

Stability is important for the design of the control system. The closed-loop transfer function from the reference signal r to the measured value y is [11]

$$G_{ry}(s) = \frac{L(s)}{1 + L(s)}. \tag{2.17}$$

Hence, the characteristic equation to find the poles of the closed-loop system can be expressed as

$$1 + L(s) = 0, \tag{2.18}$$

where $L(s)$ is the open-loop transfer function. For a system to be stable, all poles must be placed in the Left-Half Plane (LHP). This ensures that the system's response decreases over time rather than increasing without bound. The sensitivity function is a common tool for analyzing the stability and performance of control systems [11]. The sensitivity function quantifies how the system's output responds to changes in the input or system parameters. It is defined as

$$S(s) = \frac{1}{1 + L(s)}. \tag{2.19}$$

Another concept in control systems is the maximum sensitivity. This metric helps to evaluate the worst-case scenario for sensitivity across all frequencies [11].

$$M_s = \max_{\omega} |S(j\omega)| \tag{2.20}$$

where ω represents the frequency. For the desired properties of the closed-loop system presented in (2.16), it is essential to ensure that the maximum sensitivity remains within acceptable limits.

2.2.4 Bilinear Transform

The bilinear transform, also known as Tustin's method or trapezoidal rule, approximates the derivative by taking the average between the current and previous input values. Infrequency domain, this approximation looks like [14]:

$$s = \frac{2}{T_s} \cdot \frac{1 - z^{-1}}{1 + z^{-1}}. \tag{2.21}$$

For a low-pass filter of the form

$$G(s) = \frac{1}{1 + \frac{1}{\omega_c} s}, \tag{2.22}$$

its dynamics in the time domain can then be expressed as:

$$y[k] = c_1 \cdot (x[k] + x[k-1]) + c_2 \cdot y[k-1] \tag{2.23}$$

where x is the input signal and y is the output signal from the filter. The coefficients are defined by:

$$c_1 = \frac{T_s}{2\tau + T_s} \quad \text{and} \quad c_2 = \frac{2\tau - T_s}{2\tau + T_s}. \tag{2.24}$$

This formulation in (2.23) is convenient for implementing the discrete low-pass filter in code. Here, T_s denotes the sampling period and ω_c is the filter cutoff frequency. This formulation effectively preserves the frequency response characteristics, resulting in an accurate representation of the low-pass filter.

2.2.5 Padé Approximation

The Padé approximation is a method for approximating a function based on a Taylor series expansion. For function with a time delay, the dead time e^{-sL} can be rewritten as

$$e^{-sL} = e^{-s\frac{L}{2}} e^{-s\frac{L}{2}} = \frac{e^{-s\frac{L}{2}}}{e^{s\frac{L}{2}}} \tag{2.25}$$

where the nominator and denominator are replaced by their respective Taylor series of order n. The phase of the approximation is ensured to be similar to the dead time [11], using

$$G_n(s) = \frac{1 + \beta_{p,1}s + \beta_{p,2}s^2 + \cdots + \beta_{p,n}s^{n_p}}{1 + \alpha_{p,1}s + \alpha_{p,2}s^2 + \cdots + \alpha_{p,n}s^{n_p}}. \tag{2.26}$$

The coefficients $\alpha_{p,i}$ and $\beta_{p,i}$ are chosen so that the delay and $G_n(s)$ matches up to order $2n_p$ [11], as shown by

$$\frac{d^{k_p}}{ds^{k_p}} e^{-sL}|_{s=0} = \frac{d^{k_p}}{ds^{k_p}} G_n(s)|_{s=0} \qquad k_p = 1, \cdots, 2n_p. \tag{2.27}$$

The Padé approximation is useful for approximating the dead time in the system, as it captures the essential phase lag introduced by the delay while maintaining the system's realizability as a rational transfer function.

2.3 Performance Metrics

To evaluate the performance of the control strategy, some performance metrics are defined. These metrics evaluate both tracking accuracy and the ability to maintain the system output within acceptable boundaries. The following subsections describe the two primary performance indicators used in this thesis.

2.3.1 Root Mean Square Error

The Root Mean Square Error (RMSE) computes the average magnitude of the error between a predicted or controlled variable and its reference value. Given a reference

signal $r(t)$ and the corresponding measured or simulated output $y(t)$ over a time horizon of N samples, the RMSE is defined as [15]

$$\text{RMSE} = \sqrt{\frac{1}{N}\sum_{t=1}^{N}\left(y(t) - r(t)\right)^2}. \tag{2.28}$$

A lower RMSE value indicates more accurate tracking performance, showing that the control strategy effectively minimizes the deviation from the reference signal.

2.3.2 Constraint Violation Integral

As the λ-value needs to stay within some predefined limits at all times, as covered in Section 2.1.3, the constraint violation integral (CVI) is introduced as a performance metric. The CVI calculates the cumulative violation of the controlled variable outside of specified bounds. Let $y_{\min}$ and $y_{\max}$ denote the bounds for a controlled signal $y(t)$. The constraint violation metric $v(t)$ at every time step is then defined as

$$v(t) = \begin{cases} y(t) - y_{\max}, & \text{if } y(t) > y_{\max} \\ y_{\min} - y(t), & \text{if } y(t) < y_{\min} \\ 0, & \text{otherwise.} \end{cases} \tag{2.29}$$

The CVI is then computed as the sum of the absolute violations over the evaluation horizon:

$$\text{CVI} = \sum_{t=1}^{N} |v(t)|. \tag{2.30}$$

This metric penalizes both the duration and the magnitude of constraint violations. Thus, a low CVI shows that the control strategy effectively enforces operational boundaries.

2.4 Parameter Identification and Mapping

The parameters of the system are determined by mapping to an operating point, which depends on the engine's speed and load [16]. This section covers the relevant methods.

2.4.1 SQP for Prediction Error Minimization

To minimize the prediction error between the model predictions and the sensor measurements, system identification can be used. To apply this method effectively, a quantitative measure of the prediction error is required for estimating model parameters. Given input-output data $\mathbf{Z}^N$, i.e $\{u(t), y(t)\}_{t=1}^{N}$ sampled with period T_s, the cost function is formulated as [17]

$$V_N(\theta, \mathbf{Z}^N) = \frac{1}{N}\sum_{t=1}^{N} e_p^2(t, \theta) \tag{2.31}$$

where $e_p(t)$ is the prediction error between the model prediction output *equation* and the sensor measurements $y(t)$. From now on, $\mathbf{Z}^N$ will be omitted from the notation of the cost function for simplicity. The measurement $y(t)$ can be described as [17]:

$$y(t) = G(q,\theta)u(t) + H(q,\theta)e_p(t) \tag{2.32}$$

where $H(q,\theta)$ is the transfer function of the noise model, which describes how noise affects the system output, and $G(q,\theta)$ is the process model. (2.32) can be rewritten to solve for $e_p(t,\theta)$:

$$e_p(t,\theta) = H^{-1}(q,\theta)[y(t) - G(q,\theta)u(t)]. \tag{2.33}$$

If the optimization parameter θ is subject to the following inequality constraints:

$$\theta_{\min} \leq \theta \leq \theta_{\max}, \tag{2.34}$$

the resulting constrained nonlinear optimization problem will look like

$$\min_{\theta\in\mathbb{R}^3} \quad V_N(\theta) = \frac{1}{N}\sum_{t=1}^{N}[H^{-1}(q,\theta)[y(t) - G(q,\theta)u(t)]]^2 \tag{2.35}$$

$$\text{s.t} \quad \theta_{\min} \leq \theta \leq \theta_{\max}. \tag{2.36}$$

Due to the nonlinear nature of the cost function and the presence of inequality constraints, a suitable numerical optimization method is the Sequential Quadratic Programming (SQP) method. SQP solves the problem by iteratively solving quadratic programming (QP) subproblems. This method is relatively fast as convergence of the SQP method is superlinear under regularity conditions [18]. Given (2.35), SQP begins with linearizing the objective and constraints at the current iteration θ_k. The Lagrangian is then defined as

$$\mathcal{L}(\theta,\lambda,\mu) = V_N(\theta) + \lambda_{\mathcal{L}}^T(\theta_{\min} - \theta) - \mu_{\mathcal{L}}^T(\theta - \theta_{\max}) \tag{2.37}$$

where $\lambda_{\mathcal{L}}$ and $\mu_{\mathcal{L}}$ are Lagrange multipliers. The quadratic subproblem at iteration k is then [19]

$$\min_{\mathbf{d}\in\mathbb{R}^3} \quad \frac{1}{2}\mathbf{d}^T\mathbf{B}_k\mathbf{d} + \nabla\mathcal{L}(\theta,\lambda,\mu)^T\mathbf{d}, \tag{2.38}$$

$$\text{s.t} \quad \theta_{\min} - \theta_k \leq \mathbf{d} \leq \theta_{\max} - \theta_k \tag{2.39}$$

where the gradient of the Lagrangian is expressed as

$$\nabla\mathcal{L}(\theta,\lambda,\mu) = \nabla V_N(\theta) - \lambda_{\mathcal{L}} + \mu_{\mathcal{L}} \tag{2.40}$$

with $\nabla V_N(\theta)$ derived as

$$\nabla V_N(\theta) = 2\sum_{t=1}^{N}\frac{\partial}{\partial\theta}\left[H^{-1}(q,\theta)[y(t) - G(q,\theta)u(t)]\right]\cdot H^{-1}(q,\theta)[y(t) - G(q,\theta)u(t)]. \tag{2.41}$$

In (2.38), $\mathbf{d}$ is the search direction and $\mathbf{B}_k$ approximates the Hessian $\nabla^2\mathcal{L}(\theta_k, \lambda_k)$ which is often updated via the BFGS algorithm [18]. The implementation of the BFGS algorithm is beyond the scope of this thesis. The next iteration of θ is updated with

$$\theta_{k+1} = \theta_k + \alpha_k \mathbf{d}_k \tag{2.42}$$

where α_k is the step-length, which is determined by a line search on the merit function [18]:

$$\phi(\theta) = V_N(\theta) + \rho \| \max(0, \theta_{\min} - \theta) + \max(0, \theta - \theta_{\max}) \|_1 \tag{2.43}$$

where ρ is the penalty parameter. This satisfies the Armijo condition [18]:

$$\phi(\theta_k + \alpha_k \mathbf{d}_k) \leq \phi(\theta_k) + \sigma_A \alpha_k \nabla\phi(\theta_k)^T \mathbf{d}_k \tag{2.44}$$

for $0 < \sigma_A < 1$, which is important to note as this guarantees convergence of the algorithm. However, this does not guarantee convergence to the global minimum of $V_N(\theta)$, meaning that the solution found is possibly a local minimum.

2.4.2 Linear Interpolation

Interpolation is an estimation method for values between known data points. Linear interpolation is an interpolation method best used for linear functions and curves that can be approximated by a linear spline function. A desired data point (x, y) between the known data points (x_1, y_1) and (x_2, y_2) is calculated with [20]

$$y = y_1 + (y_2 - y_1)\frac{x - x_1}{x_2 - x_1} \tag{2.45}$$

which can be rewritten as

$$\frac{y - y_1}{x - x_1} = \frac{y_2 - y_1}{x_2 - x_1} \tag{2.46}$$

interpreted as the equality between the equation of the slopes of the interpolated data point and the known data point. Figure 2.4 shows an illustration of this principle.

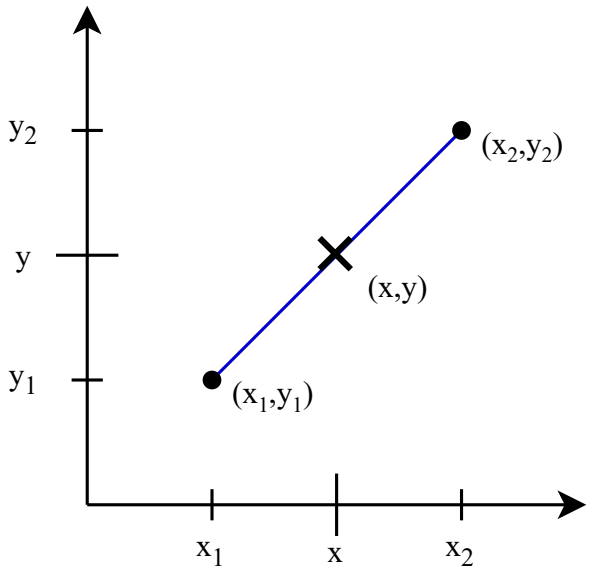

Figure 2.4: The angle of the slope between x_1, y_1 and (x, y) is equal to the slope between (x_1, y_1) and (x_2, y_2). (x_1, y_1) and (x_2, y_2) are known data points.

2.4.3 Gaussian Smoothing

Gaussian smoothing is the action of taking the weighted average of the surrounding data based on a Gaussian smoothing kernel, expressed as

$$K(x, x_j) = exp\Big(- \frac{||x - x_j||_2^2}{2\sigma^2} \Big) \tag{2.47}$$

where σ is the width of the kernel [21]. The purpose of the Gaussian kernel is to smooth local deformations, the goal is to set σ to capture all prominent spikes and dips while reducing the noise.

2.4.4 Simulated Annealing

Simulated annealing is a probabilistic optimization algorithm, [22]. Simulated annealing explores a solution space to find a global optimum by initially allowing large, random changes in the solution, which become increasingly conservative for every iteration of the algorithm.

The algorithm begins with an initial solution and a high temperature value T_{SA}. At each iteration, a new solution is generated by applying a small, random change to the current solution. If this new solution results in an improved objective value, it is accepted as the current solution. However, if the new solution is worse, it may still be accepted with a probability P_a given by the Boltzmann distribution:

$$P_a = \exp\left(-\frac{\Delta E}{T_{SA}}\right) \tag{2.48}$$

where ΔE is the increase in the objective function. This probabilistic acceptance of suboptimal solutions enables the algorithm to escape local minima and explore potential solutions more comprehensively in the early stages. This leads to simulated annealing being a suitable choice for finding the global optimum of the objective function.

As the algorithm progresses, the temperature is gradually reduced according to a cooling schedule, which controls the transition from exploration to exploitation. The temperature is then updated as follows:

$$T_{SA,k_s+1} = \alpha_t T_{SA,k_s} \tag{2.49}$$

where T_{SA,k_s} is the temperature at iteration k_s and $\alpha_t \in (0, 1)$ is the cooling rate. This schedule reduces the probability of accepting worse solutions, increasing the likelihood of convergence to a solution close to the optimum.

2.5 Chapter Summary

This chapter outlined basic ICE theory and the theoretical foundations used in the development of the control system. The Padé approximation was introduced to approximate system dead-time using rational functions. The structure and tuning of PID controllers were described, along with the Otto-Smith predictor, which compensates for time delays. Methods for parameter identification and optimization were also presented, including sequential quadratic programming, linear interpolation, smoothing techniques, and simulated annealing.

3
Methods

This chapter presents the methodology used to develop and implement the air-path lambda control system. It begins by outlining the overall control architecture, including the procedures for calculating boost pressure and fuel demand. Next, the lambda demand and feedback control strategies are described. The chapter then details the system identification process based on engine test cell data. Finally, it covers the construction of parameter maps for both the system and controller across various operating conditions.

3.1 Control Structure

The control structure can be divided into two main parts, as shown in Figure 3.1. Section 3.2 presents one part, which includes the feedforward calculations for fuel and boost pressure. The second part is described in Section 3.3, which consists of the controller for air input. The structure does not consider EGR dynamics.

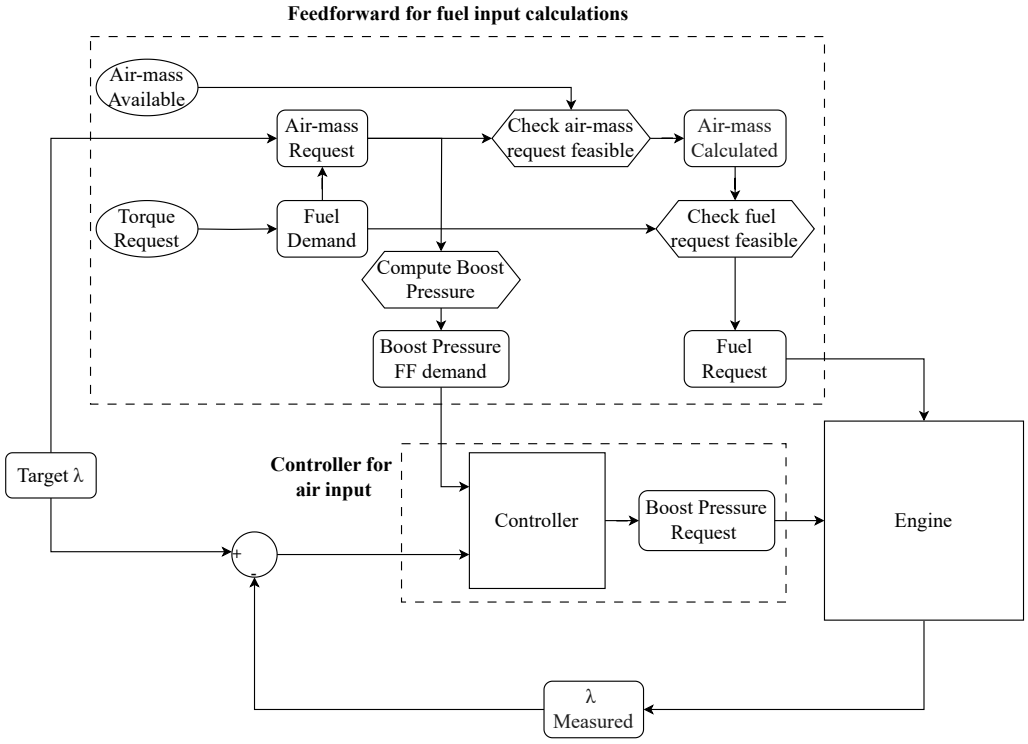

Figure 3.1: Lambda control structure.

The external signals required by the system are the current air-mass flow $\dot{m}_{air}$ and the fuel flow demand to achieve a specific torque $\dot{m}_{fuel}$. These, together with the target λ, are used to compute a fuel request for the fuel injector, as well as a boost pressure feedforward request.

The controller uses the computed boost pressure feedforward request and the λ-error, which is the difference between the target λ and the measured λ, to determine the necessary boost pressure for achieving the desired value of λ.

3.2 Feedforward Calculations

In this section, the methods for determining the appropriate boost and fuel demands will be presented.

3.2.1 Boost Request Calculations

To calculate the air-mass flow, $\dot{m}_{air}$, for the corresponding fuel flow, $\dot{m}_{fuel}$, the stoichiometric AFR is the deciding factor. Existing software is used to calculate the fuel flow request from the torque demand. Thereafter, the air-mass flow is calculated for stoichiometric combustion as:

$$\dot{m}_{air,stoic} = AFR_{stoic} \cdot \dot{m}_{fuel}. \tag{3.1}$$

Given $\dot{m}_{air,stoic}$, an air-mass flow request ($\dot{m}_{air,req}$) is calculated with the target λ as:

$$\dot{m}_{air,req} = \lambda \cdot \dot{m}_{air,stoic}. \tag{3.2}$$

The ideal gas law,

$$PV = nRT = \frac{m}{M}RT \Rightarrow \tag{3.3}$$

$$m = \frac{PVM}{RT} \tag{3.4}$$

can be used to calculate the boost pressure request,$p_{i,req}$. The boost pressure request is calculated from the current input air-mass flow, $\dot{m}_{air}$, and the requested air-mass flow, $\dot{m}_{air,req}$. The ratio between the requested and available air mass can be expressed as

$$\frac{m_{air,req}}{m_{air}} = \frac{\dot{m}_{air,req} \cdot t + m_{air,0}}{\dot{m}_{air} \cdot t + m_{air,0}}. \tag{3.5}$$

where m_0 is the initial mass. As only the ratio between the mass flows is of interest and the time period (t) can be chosen arbitrarily, $m_{air,0}$ is assumed to be zero. Thus, (3.5) can be simplified to

$$\frac{m_{air,req}}{m_{air}} = \frac{\dot{m}_{air,req}}{\dot{m}_{air}}. \tag{3.6}$$

The ratio between $\dot{m}_{air,req}$ and $\dot{m}_{air}$ can then be written using (3.4), assuming that T_i stays relatively constant over short time intervals as

$$\frac{\dot{m}_{air,req}}{\dot{m}_{air}} = \frac{m_{air,req}}{m_{air}} = \frac{\frac{VM}{R} \cdot \frac{p_{req}}{T_{in}}}{\frac{VM}{R} \cdot \frac{p_i}{T_{in}}} = \frac{p_{req}}{p_i}. \tag{3.7}$$

The requested boost pressure can then be determined as:

$$p_{req} = p_i \frac{\dot{m}_{air,req}}{\dot{m}_{air}}. \tag{3.8}$$

When using EGR, additional flow is provided from the unburnt air in the exhaust gases.

3.2.2 Fuel Quantity Request Calculations

Due to the VGT spool time during transient operations, the $\dot{m}_{air,req}$ is not guaranteed for every time instant. Therefore, the current air mass flow $\dot{m}_{air}$ is used for the calculations. Using $\dot{m}_{air}$ and the given $\dot{m}_{fuel}$, λ_{in} is calculated and checked. The AFR is too fuel-rich for hydrogen combustion if the results yield a λ below the minimum possible relative AFR for hydrogen combustion λ_{min}. Subsequently, it was ensured that the current relative AFR was not larger than the maximum possible λ_{max}. These limits were covered in more detail in Section 2.1.3. The check calculates λ_{feas}, to ensure feasibility:

$$\lambda_{in} = K \cdot \frac{\dot{m}_{air}}{\dot{m}_{fuel}} \cdot \frac{1}{AFR_{stoic}} \tag{3.9}$$

$$\lambda_{feas} = \min(\max(\lambda_{in}, \lambda_{min}), \lambda_{max}). \tag{3.10}$$

In (3.10) K is the static gain in (3.13). The final fuel flow request, $\dot{m}_{fuel,feas}$, is calculated from the λ_{feas} given by (3.9) as

$$\dot{m}_{fuel,feas} = \frac{\lambda_{feas} \cdot AFR_{stoic}}{\dot{m}_{air}}. \tag{3.11}$$

The calculated $\dot{m}_{fuel,feas}$ is the input for the fuel injector.

3.3 Lambda Control

The following subsections cover the implementation of the lambda controller. An overview of the feedback strategy is presented in Figure 3.2.

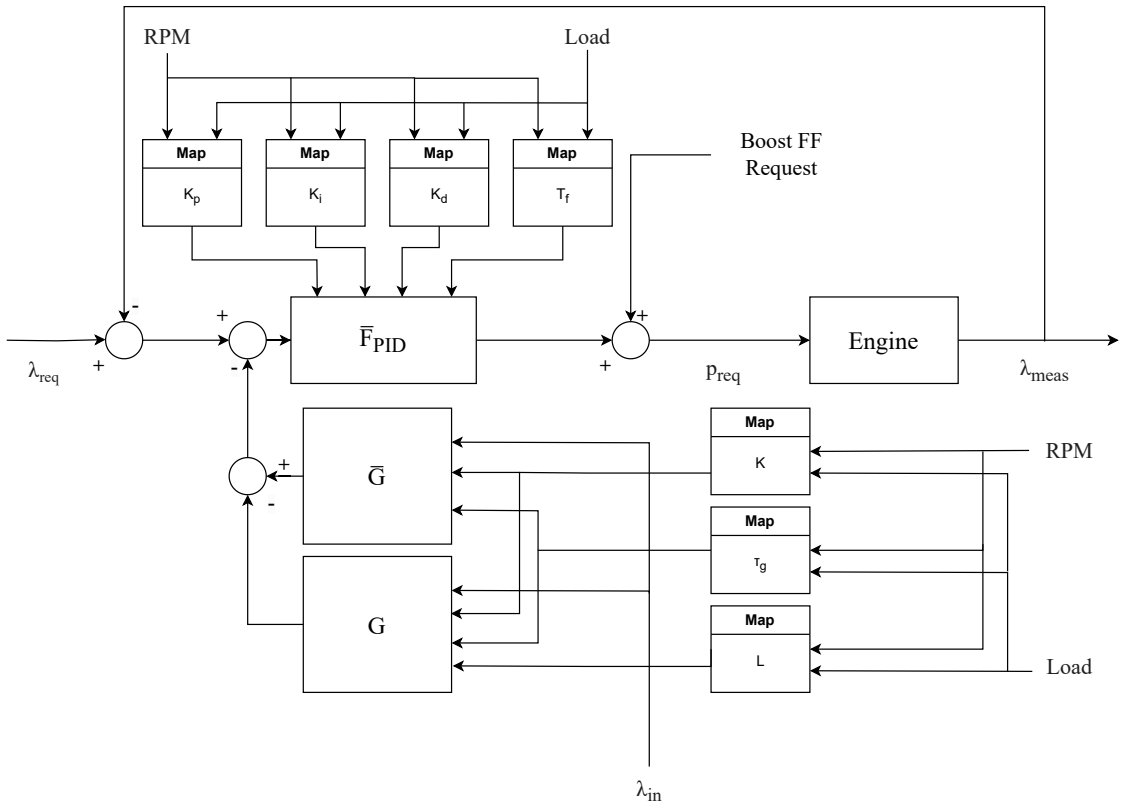

Figure 3.2: Lambda feedback strategy overview

The implementation consists of a strategy for determining a target λ, followed by the λ model response, leading to a feedback strategy. The PID controller parameters are dependent on RPM and load, meaning that the controller is constructed for each operating point using parameter maps. RPM and load-dependent parameter maps are also implemented for the system parameters, for estimating the model response at all operating points. The construction of all the RPM and load-dependent parameter maps is described in Section 3.4.

3.3.1 Target Lambda

The desired AFR is set to a constant value, which is a simplified approach to implement a target demand λ. λ is chosen to minimize NO_x emissions while optimizing engine performance, i.e., satisfying as many torque requests as possible. As mentioned in Section 2.1.3, a good choice for λ is found to be greater than 2 but less than 2.7 for stable combustion with low emissions. It is mentioned that a lean AFR will sacrifice engine power; therefore, λ is set to two. Temporary deviation from the target λ is permitted during transient operations to maintain performance.

3.3.2 Lambda Feedback Strategy

In this subsection, the controller for air input, as shown in Figure 3.1, will be analyzed in detail. The feedback strategy shown in Figure 3.2 results in an Otto-Smith

predictor mentioned in Section 2.2.2. A First-Order Plus Dead Time (FOPDT) model is used to model the plant. The dynamics from the cylinder relative AFR (λ) to the measured relative AFR (λ_{meas}) is expressed with the transfer function [23]

$$G(s) = \bar{G}(s)e^{-Ls} \tag{3.12}$$

$$\bar{G}(s) = \frac{K}{1 + s\tau_g} \tag{3.13}$$

where $\bar{G}(s)$ is the transfer function without dead time. The constants characterizing the model are the static gain K, the transport delay for the gas L, and the gas dynamics time constant τ_g. Applying the Tustin approximation for s and substituting the expression in (2.21) into (3.12) and the delay e^{-Ls} with z^{-d} where $d = \lceil \frac{L}{T_s} \rceil$

$$G(z) = \frac{K}{1 + \left(\frac{2}{T_s} \cdot \frac{1-z^{-1}}{1+z^{-1}}\right)\tau_g} z^{-d}. \tag{3.14}$$

Simplifying the expression yields the following discrete-time transfer function:

$$G(z) = \frac{KT_s(1 + z^{-1})}{(T_s + 2\tau_g) + (T_s - 2\tau_g)z^{-1}} z^{-d}. \tag{3.15}$$

The plant model was approximated using the mapped values of K, L, and τ_g, which were derived using the methods presented in Section 3.4. The input to the approximated plant is λ_{in}, which is calculated according to (3.9).

A PID controller, represented by $\bar{F}_{PID}$, was implemented in accordance with Section 2.2.1, and the controller gain was determined by the maps obtained in Section 3.4.3. $\bar{F}(s)$ is expressed as in (2.9) with $\zeta = 0.7$ and $\beta = 5$, according to [11]. Combinations of τ and K_i were implemented to ensure sufficient stability properties. Specifically, $M_s \leq 1.7$ is desired with maximized K_i [11]. The output signal from the PID controller is added to the boost-pressure feedforward demand obtained in Section 3.2.1. Lastly, the measured relative AFR is used for feedback. The PID-controller output is also limited as follows:

$$90 \leq p_{req} \leq 400. \tag{3.16}$$

These limits were chosen because the boost pressure in the intake manifold p_i cannot exceed 400 kPa. Furthermore, p_i cannot fall significantly below atmospheric pressure as this may lead to oil leakage. Anti-windup is used to avoid the build-up of integral action in the PID-controller which increases when the desired boost pressure is outside of the bounds 3.16. This is done by enforcing bounds on the integral term to ensure that the combined output of the feedforward, proportional, and integral components does not exceed the controller's minimum and maximum limits.

3.4 Parameter Map Creation

This section covers the creation and implementation of parameter maps for the process model presented in (3.12), as well as for the PID controller. The reason for creating these maps instead of computing the values dynamically is to reduce computational complexity.

3.4.1 Data Preprocessing

Due to noisy measurements of λ_{meas} and the signals used to calculate λ_{in}, preprocessing is needed before system identification is performed as described in Section 3.4.2. Thus, Gaussian smoothing is applied to the measured lambda as described in Section 2.4.3. In order to have a good trade-off of retaining the dead-time and time-constant characteristics and reducing noise, the kernel width of the Gaussian distribution in (2.47) is chosen as:

$$\sigma_{prep} = 5. \tag{3.17}$$

3.4.2 System Identification

Engine test cycle data $\mathbf{Z}^N$, where engine performance was recorded for various operating points, are used for system identification to estimate model parameters. The operating points consisted of various combinations of RPM and load. The operating cycle is shown in Figure 3.3.

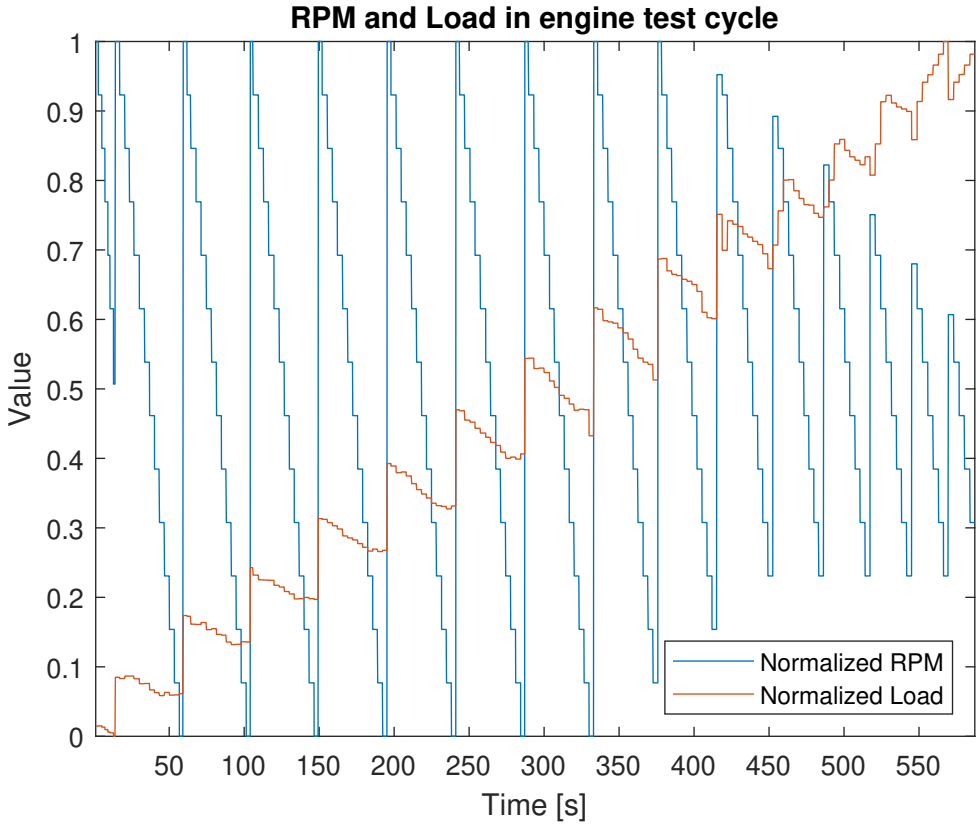

Figure 3.3: Test cycle used for system identification. The cycle is normalized for privacy reasons.

The data used for system identification was

$$\mathbf{Z}^N = \{u(t), y(t)\}_{t=1}^N = \{\lambda_{in}(t), \lambda_{meas}(t)\}_{t=1}^N \tag{3.18}$$

where $\lambda_{in}(t)$ was calculated from the current air mass flow $\dot{m}_{air}$ and the fuel mass flow $\dot{m}_{fuel}$, measured by the test rig in the same way as in (3.9). MATLAB's System Identification Toolbox was used to solve the system identification problem. Considering a system modeled by (3.12) and a noise model that is estimated by the algorithm, the parameter vector for the SQP described in Section 2.4.1 is defined as

$$\theta = [K, \tau_g, L]^\top. \tag{3.19}$$

The inequality constraints for θ are

$$\begin{bmatrix} 0.9 \\ 0 \\ 0 \end{bmatrix} \leq \theta \leq \begin{bmatrix} 1.1 \\ 2 \\ 2 \end{bmatrix}. \tag{3.20}$$

The constraints were chosen based on knowledge of the physical system. Ideally, K should be equal to one as λ_{in} should propagate to the lambda-sensor. However, due to inaccuracies in $\dot{m}_{air}$ and $\dot{m}_{fuel}$ used to calculate λ_{in}, the static gain is constrained by a range of 1 ± 0.1. The constraints on τ_g and L were determined based on observations of lambda-transient behavior. The optimization algorithm has a function

tolerance f_{tol} to determine when to terminate based on minimal change in the cost function $V_N(\theta)$ between iterations, i.e., stopping if

$$f_{tol} \geq V_N(\theta_{k+1}) - V_N(\theta_k). \tag{3.21}$$

Similarly, the step tolerance s_{tol} controls termination based on change in the parameter vector θ, stopping the iterations if the step size becomes sufficiently small, i.e.

$$s_{tol} \geq \|\theta_{k+1} - \theta_k\|. \tag{3.22}$$

The function and step tolerance were chosen as

$$f_{tol} = 10^{-6} \tag{3.23}$$
$$s_{tol} = 10^{-9} \tag{3.24}$$

as well as setting the maximum number of iterations for the algorithm to 10^4. The SQP algorithm was run for each operating point separately, mapping the parameters to each RPM-load combination in the dataset.

3.4.3 PID Parameter Mapping and Tuning Methodology

From the criteria $M_s \leq 1.7$ and having K_i as large as possible, covered in Sections 2.2.2 and 2.2.3, K_i and τ are calculated using simulated annealing as described in Section 2.4.4. Having the objective function to be minimized defined as:

$$f(K_i, \tau) = \begin{cases} -K_i, & \textbf{if} \quad M_s(K_i, \tau) \leq M_{s,\max} \\ 1000, & \textbf{if} \quad M_{s,\max} < M_s(K_i, \tau), \end{cases} \tag{3.25}$$

ensures that K_i is maximized. The maximum sensitivity M_s is denoted $M_s(K_i, \tau)$ to highlight which parameters affect its value (having $\beta = 5$ and $\zeta = 0.7$ fixed as covered in Section 3.3.2) and the maximum allowed M_s is denoted $M_{s,\max}$. To obtain M_s, a fifth-order Padé approximation (see Section 2.2.5) is applied to the system presented in (3.12). If M_s is larger than $M_{s,\max}$, it is heavily penalized, making the probability of accepting such a solution improbable, as seen in (2.48) with ΔE defined as:

$$\Delta E = f(K_{i,old}, \tau_{old}) - f(K_{i,new}, \tau_{new}) \tag{3.26}$$

and the initial temperature T_0 and cooling rate α_t was set to

$$T_{SA,0} = 1 \tag{3.27}$$
$$\alpha_t = 0.95. \tag{3.28}$$

This was found to give relatively fast and accurate convergence. In this thesis, $M_{s,\max}$ was chosen as

$$M_{s,\max} = 1.2, \tag{3.29}$$

as it aligns with the desire to keep $M_s \leq 1.7$, and also allows for a bit less overshoot and more robust control while maintaining a short rise time. If the algorithm fails to find a solution that has a solution with $M_{s,\max} - M_s < tol$, where $tol = 0.5$ is the tolerance for the solution, the algorithm is executed again for that operating point until a satisfactory solution is found.

Using the calculated K_i and τ maps, the corresponding maps for K_p and K_d must be determined. This is done using (2.10)-(2.14), with $\beta = 5$ and $\zeta = 0.7$. From (2.12),

$$T_f = \frac{\tau}{5}. \tag{3.30}$$

For the derivative gain filter constant, a map is created using (3.30) for every value of τ. Using (2.10):

$$1.4\tau = T_i + T_f. \tag{3.31}$$

Plugging in (3.30) in (3.31):

$$1.4\tau = T_i + \frac{\tau}{5} \Rightarrow \tag{3.32}$$

$$T_i = 1.2\tau. \tag{3.33}$$

Rewriting (2.11) and plugging in (3.33) and (3.30)

$$T_d = \left(\frac{\tau^2}{T_i} - T_f\right) \Rightarrow \tag{3.34}$$

$$T_d = \frac{\tau^2}{1.2\tau} - 0.2\tau = \frac{19}{30}\tau. \tag{3.35}$$

Having expressed T_i and T_d in terms of τ, they are finally put in (2.13) and (2.14) giving:

$$K_i = \frac{5K_p}{6\tau} \tag{3.36}$$

$$K_d = \frac{19K_p\tau}{30}. \tag{3.37}$$

Since K_i and τ are the known variables, (3.36) is rewritten to solve for K_p:

$$K_p = \frac{6\tau K_i}{5}. \tag{3.38}$$

Using (3.38) and (3.37), maps were created for all combinations of RPM and load using the reduced maps for K_i and τ. Once the maps are created, they are slightly smoothed to compensate for inaccuracies of Simulated Annealing using Gaussian Smoothing with $\sigma_{PID} = 2$.

3.4.4 Map Structure

The map structure is two-dimensional, one axis is engine speed in RPM, and the other is the engine load in Nm. The mapped parameters are K, L, and τ_g from the model described in (3.12) and (3.13). Simulink lookup tables are used for the map implementation, with RPM on the x-axis and the torque on the y-axis. As seen in Figure 3.3, not all possible combinations of RPM and load are present in the dataset. Hence, after the system identification described in Section 3.4.2, the maps contain some empty cells as illustrated in the example map of L in Table 3.1.

Load \ RPM	$\mathbf{rpm}_1$	$\mathbf{rpm}_2$	$\mathbf{rpm}_3$	$\mathbf{rpm}_4$
$\mathbf{load}_1$	$L_{(1,1)}$	$L_{(1,2)}$	$L_{(1,3)}$	
$\mathbf{load}_2$	$L_{(2,1)}$		$L_{(2,3)}$	$L_{(2,4)}$
$\mathbf{load}_3$		$L_{(3,2)}$		$L_{(3,4)}$
$\mathbf{load}_4$	$L_{(4,1)}$			$L_{(4,4)}$

Table 3.1: Example map showing engine load on the y-axis and RPM on the x-axis, with mapped parameter L.

The empty cells in Table 3.1 indicate missing data. The maps for τ_g and K have the same structure.

3.4.5 Interpolation

A functioning map requires the missing values in Table 3.1 to be filled; the linear interpolation method was used as described in Section 2.4.2. After interpolation, the map structure looks like

Load \ RPM	$\mathbf{rpm}_1$	$\mathbf{rpm}_2$	$\mathbf{rpm}_3$	$\mathbf{rpm}_4$
$\mathbf{load}_1$	$L_{(1,1)}$	$L_{(1,2)}$	$L_{(1,3)}$	
$\mathbf{load}_2$	$L_{(2,1)}$	$L_{(2,2),i}$	$L_{(2,3)}$	$L_{(2,4)}$
$\mathbf{load}_3$	$L_{(3,1),i}$	$L_{(3,2)}$	$L_{(3,3),i}$	$L_{(3,4)}$
$\mathbf{load}_4$	$L_{(4,1)}$	$L_{(4,2),i}$	$L_{(4,3),i}$	$L_{(4,4)}$

Table 3.2: Example map showing engine load on the y-axis and RPM on the x-axis, with mapped parameter L after interpolation.

In Table 3.2, cells indexed with i indicate interpolated values. Values that cannot be linearly interpolated, e.g. the top right cell value in Table 3.2, are filled with the nearest value on the x-axis as shown below.

Load \ RPM	$\mathbf{rpm}_1$	$\mathbf{rpm}_2$	$\mathbf{rpm}_3$	$\mathbf{rpm}_4$
$\mathbf{load}_1$	$L_{(1,1)}$	$L_{(1,2)}$	$L_{(1,3)}$	$L_{(1,3)}$
$\mathbf{load}_2$	$L_{(2,1)}$	$L_{(2,2),i}$	$L_{(2,3)}$	$L_{(2,4)}$
$\mathbf{load}_3$	$L_{(3,1),i}$	$L_{(3,2)}$	$L_{(3,3),i}$	$L_{(3,4)}$
$\mathbf{load}_4$	$L_{(4,1)}$	$L_{(4,2),i}$	$L_{(4,3),i}$	$L_{(4,4)}$

Table 3.3: Example map showing engine load on the y-axis and RPM on the x-axis, with mapped parameter L after having replaced missing values.

The choice of method to fill the remaining missing values after interpolation is motivated by the fact that the values in question lie on the edges of the map, where the engine is unlikely to operate. Therefore, the accuracy of those values is not prioritized, and the nearest value on the x-axis is a reasonable guess for the missing data.

3.4.6 Smoothing

Due to noise and errors made by the optimization algorithm, e.g., getting stuck at a local minimum, the maps may appear noisy. Assuming that the relations between load and RPM are smooth, Gaussian smoothing is applied as described in Section 2.4.3. The table structure will be preserved in the smoothed map.

Load \ RPM	$\mathbf{rpm}_1$	$\mathbf{rpm}_2$	$\mathbf{rpm}_3$	$\mathbf{rpm}_4$
$\mathbf{load}_1$	$L_{(1,1),s}$	$L_{(1,2),s}$	$L_{(1,3),s}$	$L_{(1,3),s}$
$\mathbf{load}_2$	$L_{(2,1),s}$	$L_{(2,2),i,s}$	$L_{(2,3),s}$	$L_{(2,4),s}$
$\mathbf{load}_3$	$L_{(3,1),i,s}$	$L_{(3,2),s}$	$L_{(3,3),i,s}$	$L_{(3,4),s}$
$\mathbf{load}_4$	$L_{(4,1),s}$	$L_{(4,2),i,s}$	$L_{(4,3),i,s}$	$L_{(4,4),s}$

Table 3.4: Example map showing engine load on the y-axis and RPM on the x-axis, with mapped parameter L after interpolation and smoothing.

In Table 3.4, cells indexed with s indicate smoothed map values. The kernel width for the smoothing was chosen as $\sigma_{param} = 4$, which gives a good trade-off between reducing noise while not obscuring important features, often caused by over-smoothing.

3.4.7 Map Size Reduction

The original map sizes are inherently pretty large due to a large number of possible combinations of RPM and load. Due to memory constraints on the ECU, the map sizes need to be reduced. Both axes are constructed with a predetermined number of data points, selected within the range of possible RPM and torque. Using Table 3.4 as an example of how the map looked before the size reduction, the reduced map could look like Table 3.5.

RPM / Load	$\mathbf{rpm}_1$	$\mathbf{rpm}_3$
$\mathbf{load}_2$	$L_{(2,1),s}$	$L_{(2,3),s}$
$\mathbf{load}_4$	$L_{(4,1),s}$	$L_{(4,3),i,s}$

Table 3.5: Reduced example map showing engine load on the y-axis and RPM on the x-axis, with mapped parameter L.

In the implementation, a map size of 9×9 was chosen to balance detail and storage. After this operation is performed, the maps are ready to be configured in the Simulink model. When the maps are implemented, the software will automatically interpolate the parameter values outside the limits of the mapped RPM and torque values or in between the mapped values.

3.5 Chapter Summary

This chapter outlines the control structure for the air-path lambda controller, dividing it into a feedforward part for fuel input and a feedback controller for air input. Methods for calculating boost pressure and fuel demands are detailed, followed by methods for the identification of system parameters using engine test data. The chapter also covers the creation of parameter maps, including data preprocessing, interpolation, smoothing, and map size reduction to meet ECU constraints.

4

Results

This chapter presents the outcomes of the parameter estimation, controller gain scheduling, closed-loop stability analysis, and controller performance evaluation. First, parameter maps for the key model parameters and PID-controller gains are derived across the engine's operating range. Following this, the closed-loop stability of the system is analyzed. Finally, the developed controller is evaluated under various test cases, comparing lambda tracking, torque tracking, and fuel consumption against a baseline control strategy. Additional analyses consider the effects of enabling EGR and disabling the dead-time compensator.

4.1 Parameter Maps

This section presents the resulting maps for the estimated model parameters and controller gains.

4.1.1 Model Parameters

Computing the model parameter maps as described in Section 3.4, the maps for K, τ_g, and L are found.

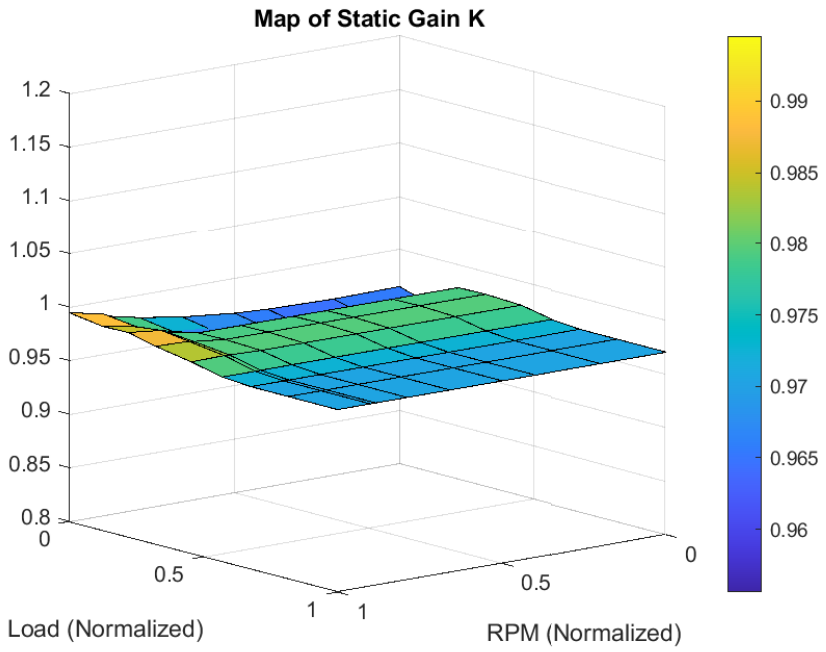

Figure 4.1: Map of static gain for different loads and RPM

In Figure 4.1, the parameter map for the static gain K is presented and is observed to be close to 1 for all RPM and loads, but always slightly below. Next, the parameter map for the time constant τ_g is presented.

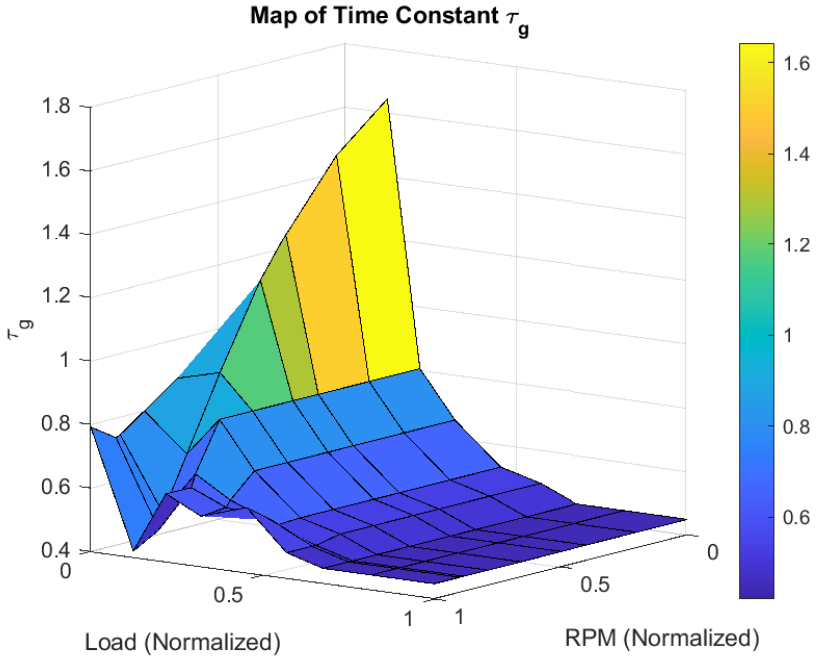

Figure 4.2: Map of gas transport time constant for different loads and RPM

In Figure 4.2, τ_g is observed to be highest when the RPM and load are low, and the value decreases the higher the engine speed and torque. It is also noted that τ_g is

slightly more dependent on load than RPM. Lastly, the map of the dead time L is presented.

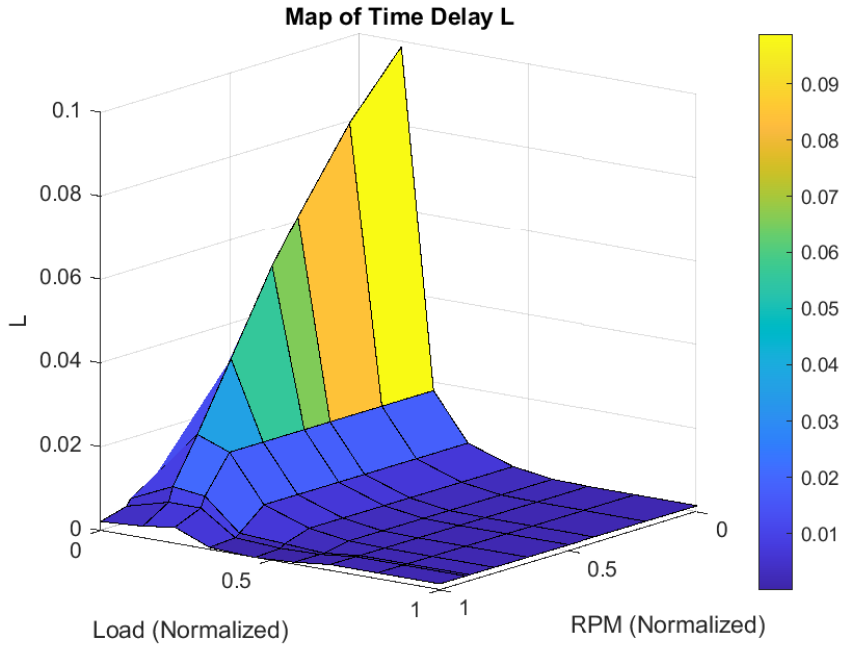

Figure 4.3: Map of gas transport dead time for different loads and RPM

In Figure 4.3, the map exhibits similar behavior to that of the map for τ_g. Again, the parameter value is highest when the load and RPM are low and gradually decreases as the load and RPM increase. The estimated λ is plotted using λ_{in} (calculated as in (3.9)) as input, with the help of the three estimated parameters.

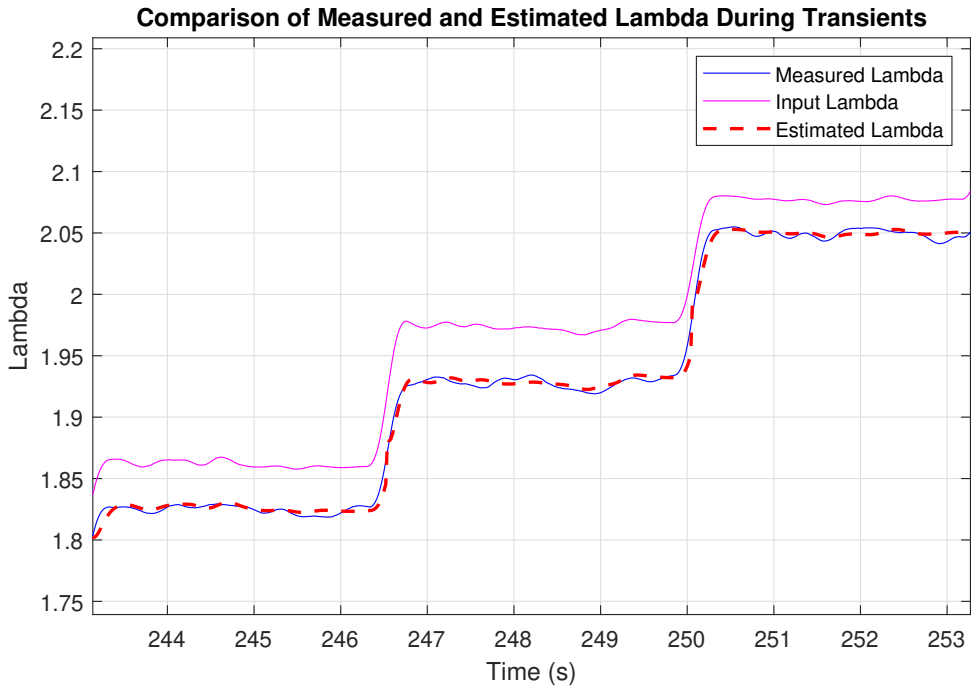

Figure 4.4: Comparison of λ_{meas}, λ_{in} and λ_{est} using mapped parameters

In Figure 4.4, it is evident that the estimated relative AFR, λ_{est}, matches the measured one quite well. Over the whole test cycle, the Root Mean Square Error (RMSE) between λ_{est} and λ_{meas} was calculated to be $RMSE_{est} = 0.02$. Given that the mean value of the measured relative AFR is $\bar{\lambda}_{meas} = 2.29$, which means that $RMSE_{est}$ is less than 1% of $\bar{\lambda}_{meas}$.

4.1.2 Controller Parameters

The PID controllers' parameters, computed as described in Section 3.4.3, are covered below. First, the map of the proportional gain K_p is presented.

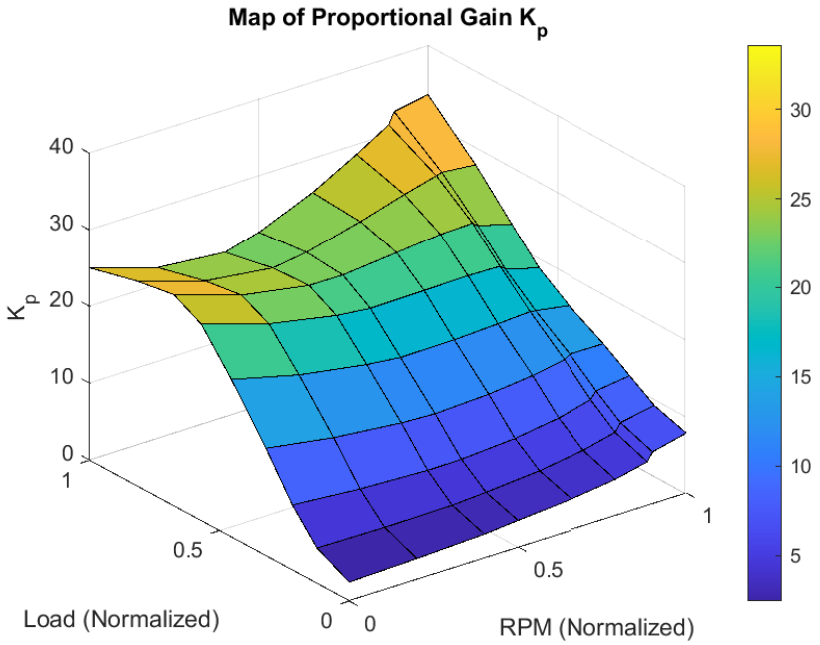

Figure 4.5: Map of proportional gain for different loads and RPM

In Figure 4.5, the maximum of the proportional gain K_p is observed to be 30 and the minimum 5. The lower values of K_p are present for low RPM and load. Increasing RPM and load, with significantly more influence on the load, is observed to increase the K_p value.

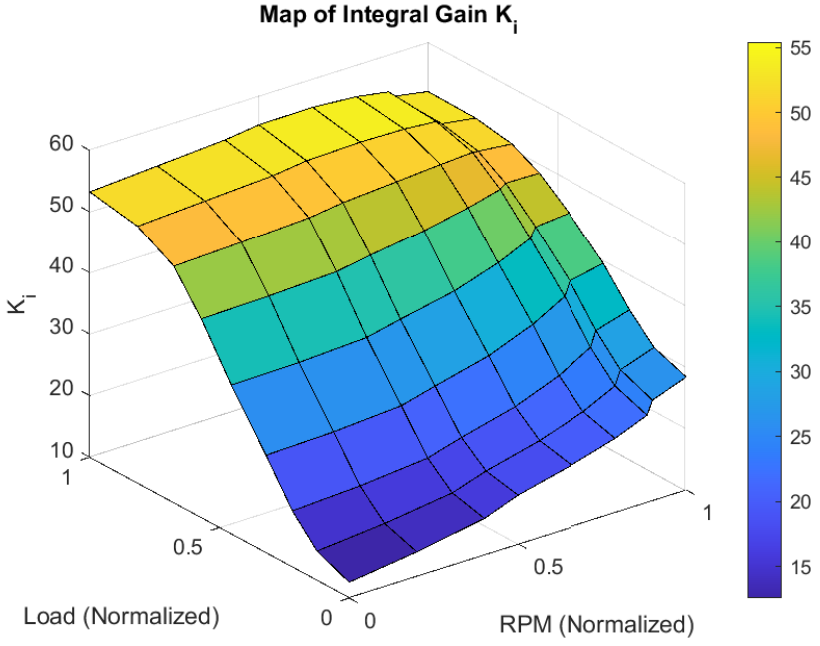

Figure 4.6: Map of integral gain for different loads and RPM

The maximum value for K_i is 55 and the minimum is 15, as noted in Figure 4.6.

The highest values of K_i are observed for the high RPM and loads. The decrease in K_i value is primarily influenced by the decrease in RPM and load, with the latter being the more significant factor.

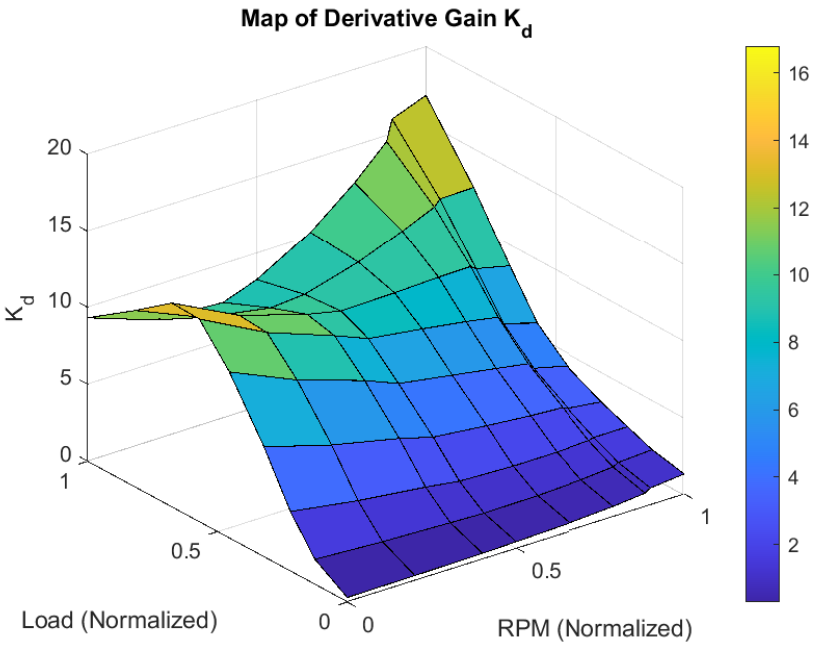

Figure 4.7: Map of derivative gain for different loads and RPM

For the derivative gain in Figure 4.7, the maximum value is observed to be at 16 and the minimum value at 2. The behavior of the derivative gain is similar in comparison with the proportional gain in Figure 4.5. Both gains increase in value as the RPM and load increase, with more weight to the load. The sensitivity to load changes is slightly higher for the derivative gain in comparison to the proportional gain, as observed in Figures 4.7 and 4.5.

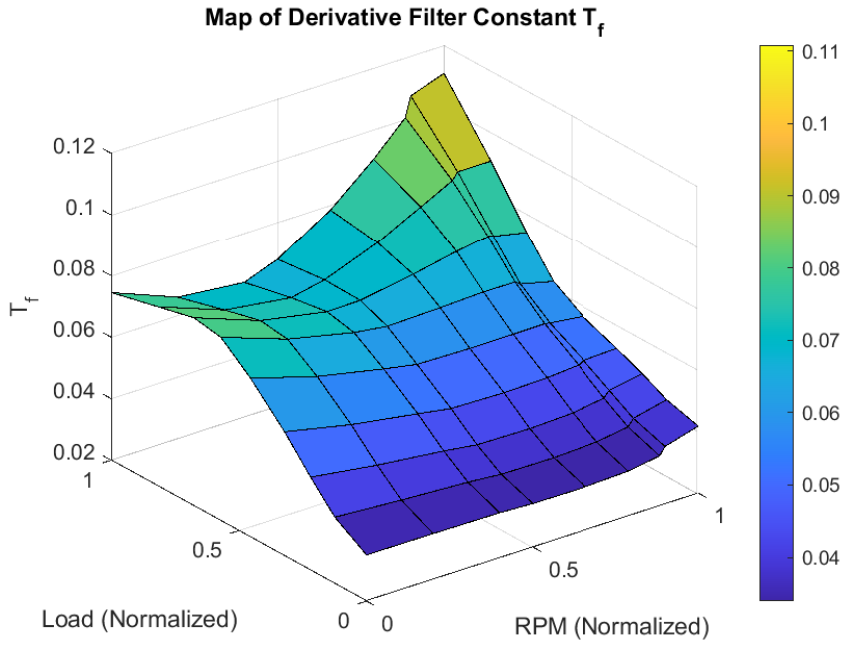

Figure 4.8: Map of derivative filter constant for different loads and RPM

In Figure 4.8, the limits of the derivative filter constant are noted at the maximum value of 0.11 and the minimum value of 0.04. The derivative filter constant value decreases as the RPM and load decrease.

4.2 Closed Loop Stability

This section covers the characteristics of the closed-loop system. In accordance with the previous sections, the controller gains and plant model constants are established to be dependent on the RPM and load of the engine.

The stability analysis is performed for the edge cases and one operating point in between (operating point 2). The edge cases are at the lowest (operating point 1) and highest (operating point 3) torque and RPM. The system behavior in the resulting analysis is assumed to be applicable for various operating points. For a complete stability analysis of all operating points, see A. The dead time observed in the results is replaced with a fifth-order Padé approximation.

First, the Bode plot of the sensitivity function S is presented and analyzed.

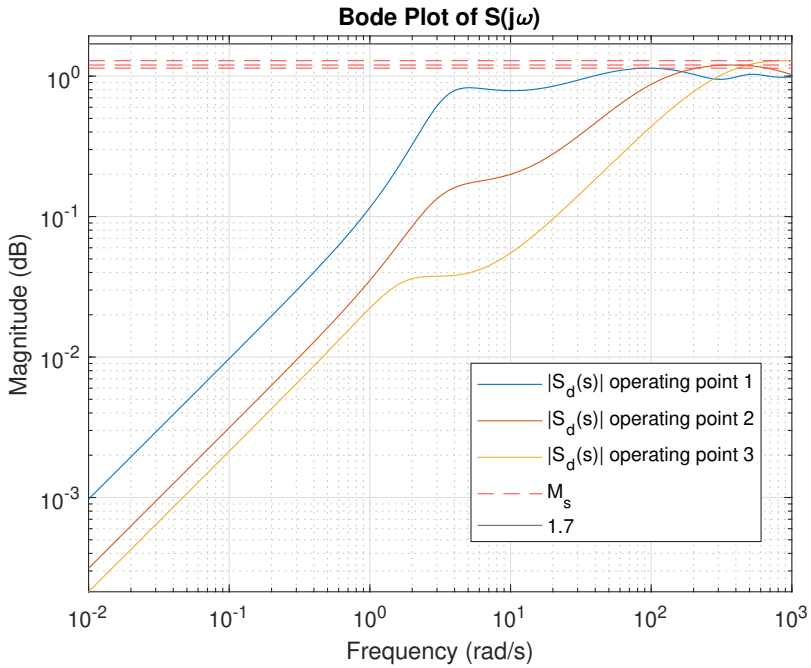

Figure 4.9: Bode plot of the sensitivity function

Analyzing Figure 4.9, the simulated annealing algorithm has evidently achieved a maximum sensitivity of around $M_s = 1.2$, as desired. The magnitude is always kept below 1.7, as discussed in 3.3.2. Next, the poles and zeros are plotted to examine the system's stability.

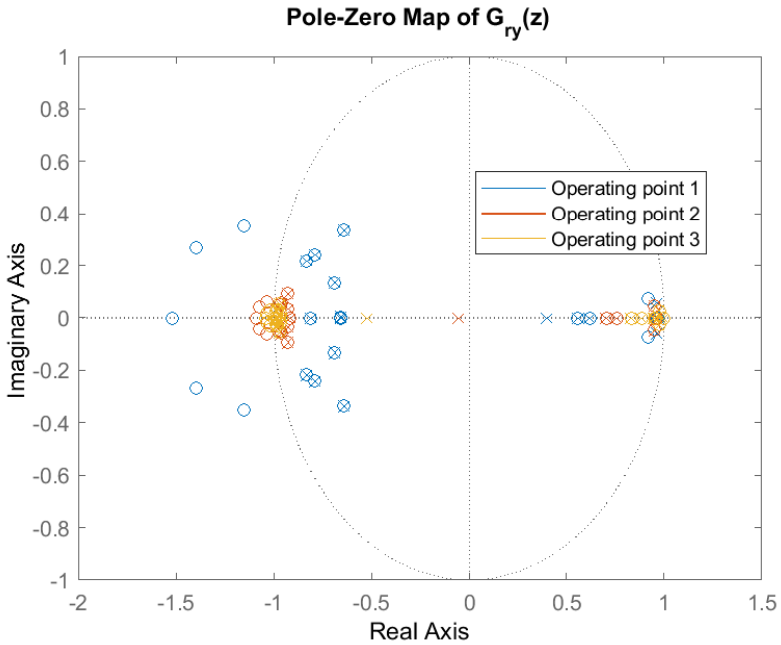

Figure 4.10: Poles (marked with ×) and zeros (marked with ∘) of the closed-loop system

In total, there are 34 poles for each operating point. Below, a closer view of the marginally stable poles is provided.

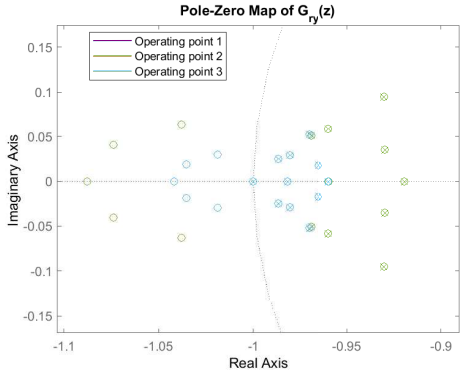

Figure 4.11: Marginally stable pole at -1 for the closed loop system

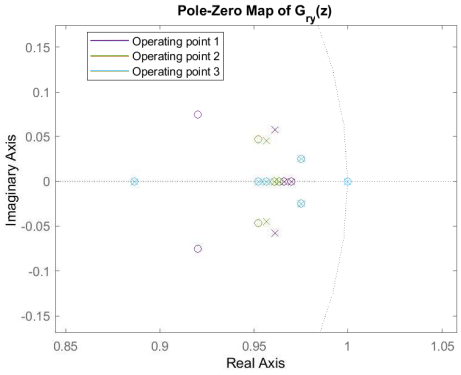

Figure 4.12: Marginally stable pole at 1 for the closed loop system

Poles at 1 and -1 can be observed, indicating marginal stability of the closed-loop system. As a result of the Padé approximation, the existing zeros enable multiple pole cancellations, resulting in a minimal realization of the discretized closed-loop system $G_{ry}(z)$.

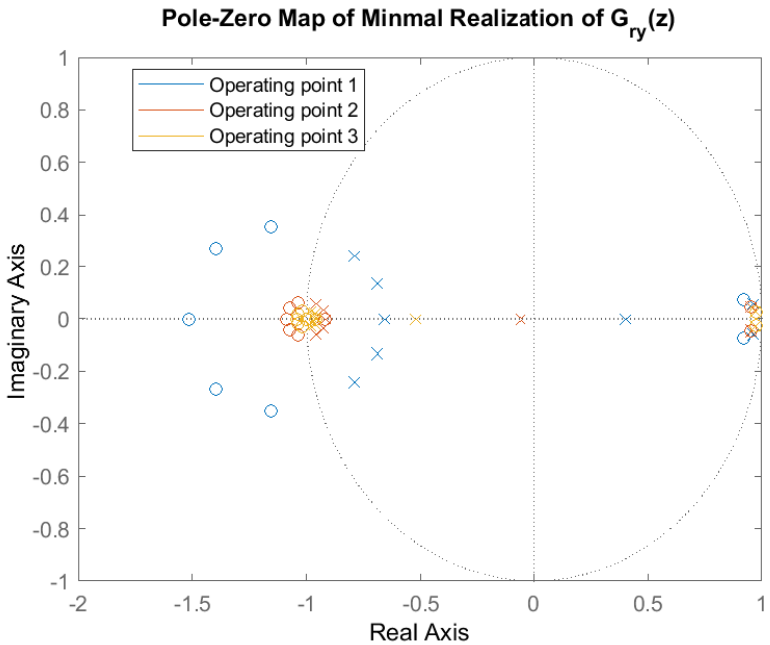

Figure 4.13: Poles and zeros for minimal realization of the closed-loop system

In Figure 4.13, the poles $\mathcal{P}$ and zeroes $\mathcal{Z}$, indexed by their respective operating point, are observed to be

$$\mathcal{P}_1 = \begin{bmatrix} -0.79 + 0.24i \\ -0.79 - 0.24i \\ -0.69 + 0.13i \\ -0.69 - 0.13i \\ -0.66 + 0.00i \\ 0.96 + 0.06i \\ 0.96 - 0.06i \\ 0.40 + 0.00i \end{bmatrix} \quad \mathcal{Z}_1 = \begin{bmatrix} 0.92 + 0.08i \\ 0.92 - 0.08i \\ -1.52 + 0.00i \\ -1.40 + 0.27i \\ -1.40 - 0.27i \\ -1.15 + 0.35i \\ -1.15 - 0.35i \\ -1.00 + 0.00i \end{bmatrix} \tag{4.1}$$

$$\mathcal{P}_2 = \begin{bmatrix} 0.96 + 0.04i \\ 0.96 - 0.04i \\ -0.06 + 0.00i \\ -0.96 + 0.06i \\ -0.96 - 0.06i \\ -0.93 + 0.04i \\ -0.93 - 0.04i \\ -0.92 + 0.00i \\ -0.92 + 0.00i \end{bmatrix} \quad \mathcal{Z}_2 = \begin{bmatrix} 0.95 + 0.05i \\ 0.95 - 0.05i \\ -1.04 + 0.07i \\ -1.04 - 0.07i \\ -1.08 + 0.04i \\ -1.08 - 0.04i \\ -1.09 + 0.00i \\ -1.00 + 0.00i \\ -0.92 + 0.00i \end{bmatrix} \tag{4.2}$$

$$\mathcal{P}_3 = \begin{bmatrix} 0.97 + 0.02i \\ 0.97 - 0.02i \\ -0.52 + 0.00i \\ -0.98 + 0.03i \\ -0.98 - 0.03i \\ -0.97 + 0.02i \\ -0.97 - 0.02i \\ -0.96 + 0.00i \\ -0.96 + 0.00i \end{bmatrix} \quad \mathcal{Z}_3 = \begin{bmatrix} 0.97 + 0.03i \\ 0.97 - 0.03i \\ -1.02 + 0.03i \\ -1.02 - 0.03i \\ -1.04 + 0.02i \\ -1.04 - 0.02i \\ -1.04 + 0.00i \\ -1.00 + 0.00i \\ -0.96 + 0.00i \end{bmatrix} \tag{4.3}$$

and the marginally stable poles observed in Figure 4.11 and Figure 4.12 are canceled out. The elimination of poles with magnitude greater than 1 indicates asymptotic stability of the system, $G_{ry}(z)$. Furthermore, the Nyquist diagram of $L(z)$ is analyzed for additional insights into the system stability.

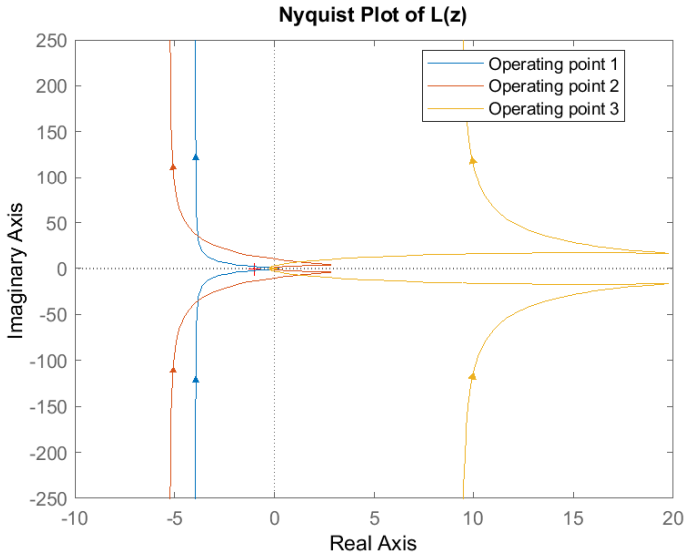

Figure 4.14: Nyquist curve of the closed-loop system

The results in Figure 4.14 present no clockwise encirclements of -1 by $L(z)$, which, in addition with the fact of no observable poles outside the unit circle in Figure 4.13, further confirms the stability of the system. Below, a step response of the closed-loop system is shown

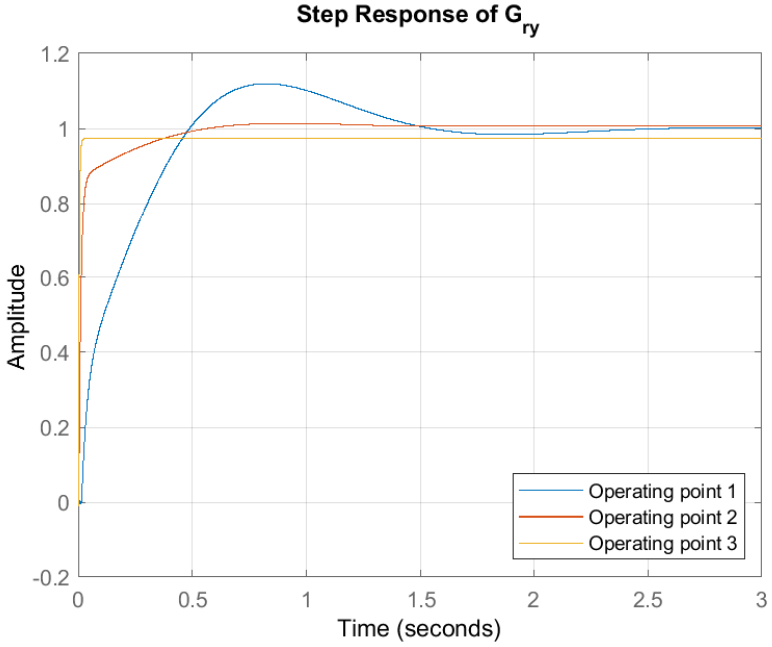

Figure 4.15: Step response of the closed-loop system

In the step response, there are no oscillations and barely any overshoot, and the rise time is quite quick for operating points 2 and 3.

4.3 Controller Performance

This section presents the performance results for the controller across various test cases, using the metrics covered in Section 2.3. The ability of the controller to achieve desired λ-tracking while keeping within its bounds is analyzed in comparison to the baseline control strategy. Next, performance in regard to torque tracking and fuel consumption is compared between the developed and baseline control strategies. Two additional test cases evaluate the developed control strategy for enabled EGR and disabled dead-time compensator. The same drive cycle was used for all test cases.

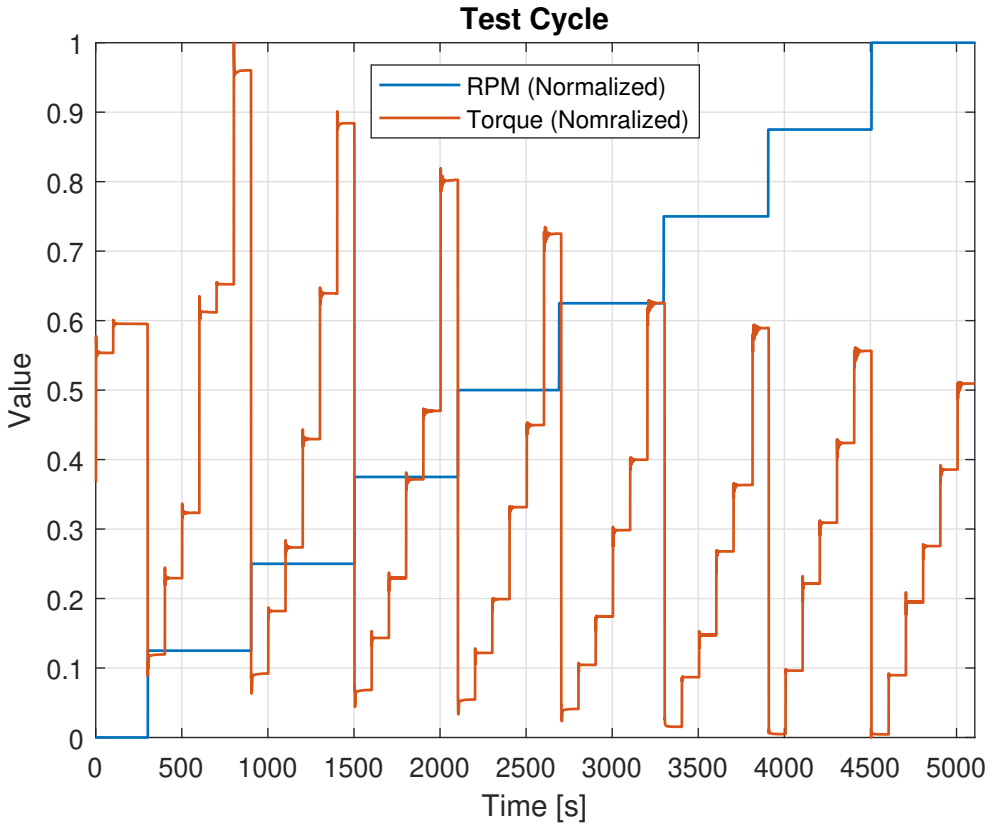

Figure 4.16: Test cycle containing different steady state scenarios

Figure 4.16 presents the drive cycle, containing a multitude of different operating points and transients, to evaluate the performance of the controller. The cycle mostly contains steady-state conditions, which is what the control strategy developed in this thesis aimed to operate under.

4.3.1 Target Lambda Tracking

The measured λ-values using lambda control and the baseline control strategy are presented in Figure 4.17.

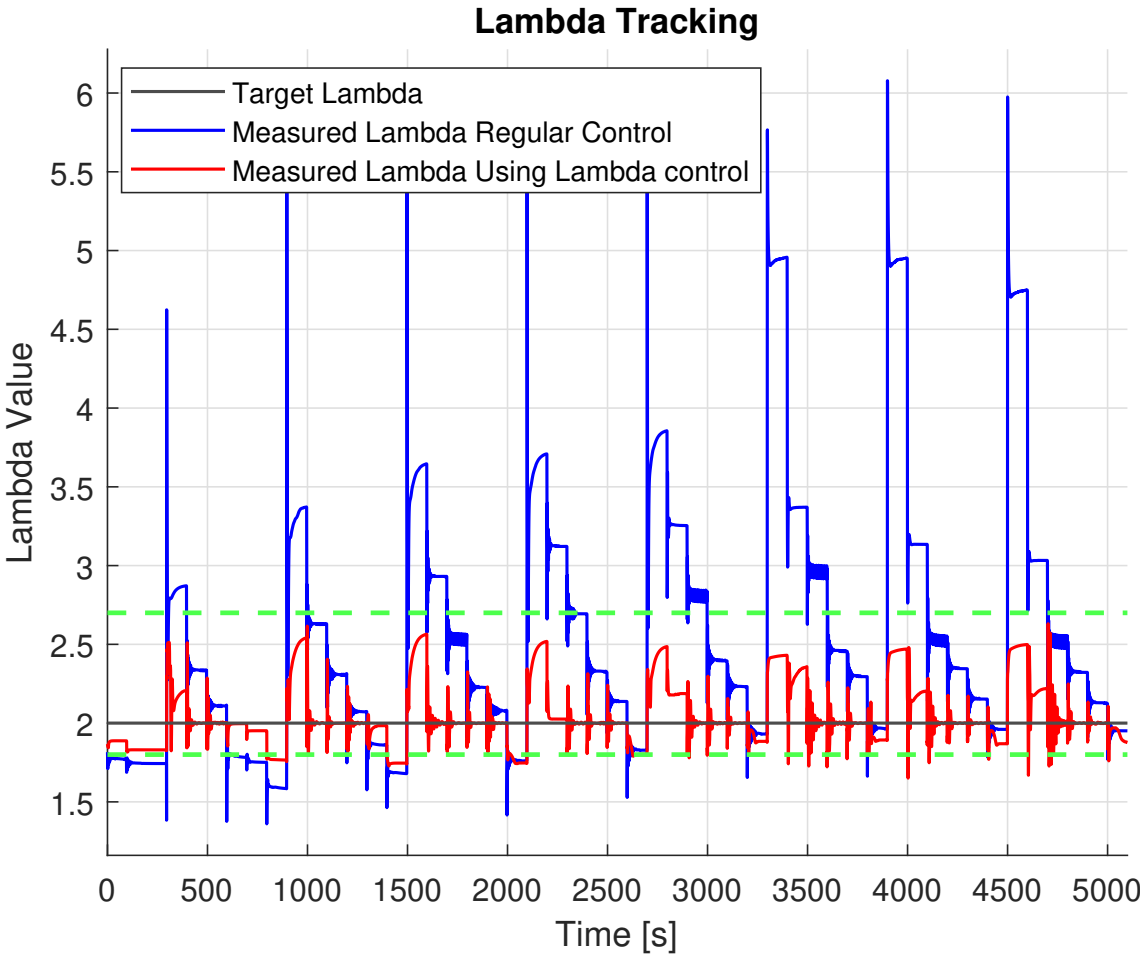

Figure 4.17: Lambda tracking comparison between the lambda control strategy and the baseline strategy

As observed in Figure 4.17, the lambda tracking strategy is exceedingly superior in comparison to the baseline strategy for maintaining lambda close to the target value and within the determined bounds. The Root Mean Square Error, described in Section 2.3.1, value for lambda using lambda control $RMSE_{\lambda,lc}$ and using regular control $RMSE_{\lambda,r}$ are

$$RMSE_{\lambda,lc} = 0.20 \qquad RMSE_{\lambda,r} = 0.98. \tag{4.4}$$

This significant improvement in lambda tracking occurs as the baseline approach considers only basic λ control, primarily mitigating combustion byproducts rather than focusing on lambda tracking. Additionally, the constraint violation integral from Section 2.3.2 for the two different strategies, CVI_{lc} and CVI_r is

$$CVI_{lc} = 27 \ [\lambda s] \qquad CVI_r = 2741 \ [\lambda s]. \tag{4.5}$$

4.3.2 Target Torque Tracking

Another performance metric evaluated was the target torque tracking capabilities of the controller, analyzed by comparing the resulting torques for different strategies with the requested torque.

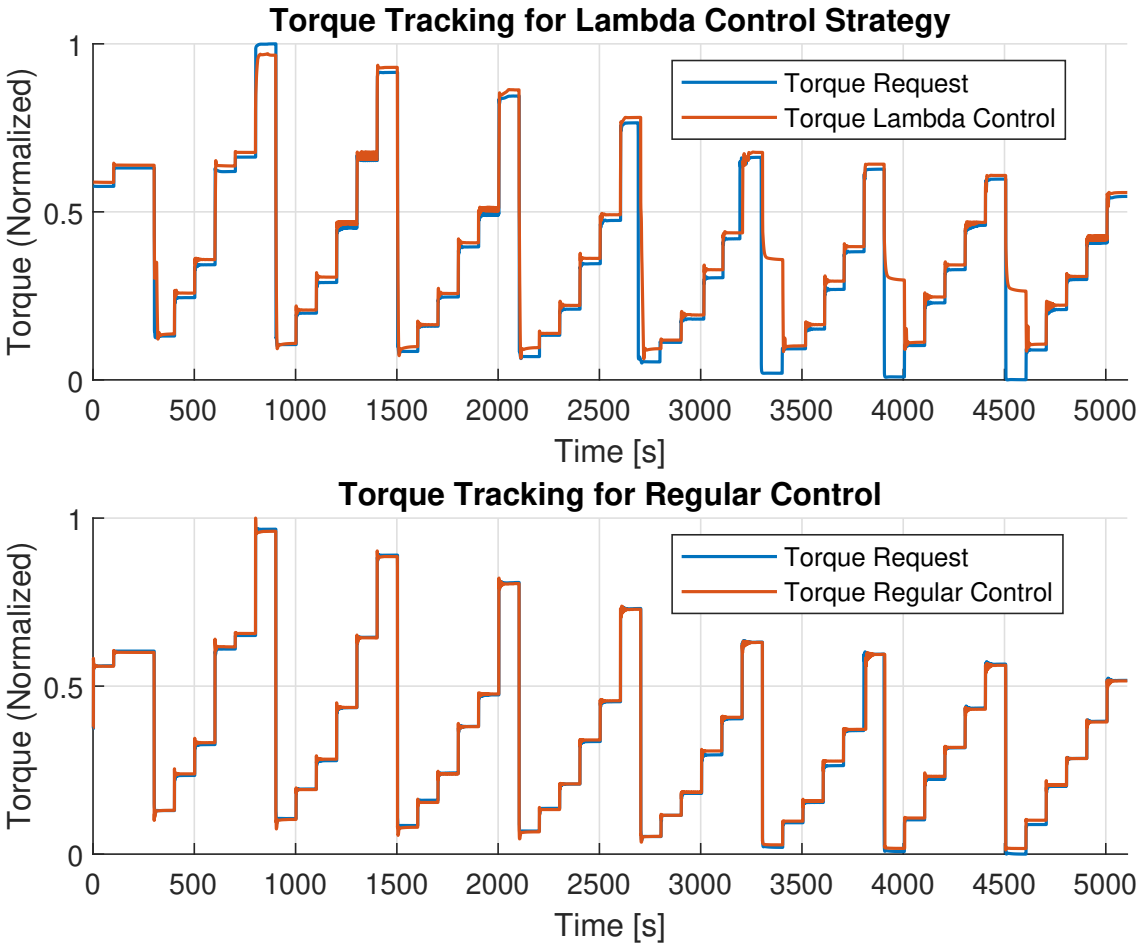

Figure 4.18: Torque tracking comparison between lambda control strategy and baseline strategy

In Figure 4.18, the lambda control strategy is inferior at torque tracking, in comparison with the baseline strategy. Due to insufficient air during high torque demands, the fuel is reduced to maintain lambda within bounds and avoid engine knocking, resulting in the inability to achieve higher torque demands. An example of unreached high torque demand can be observed at the time $600 - 900$ $[s]$. Instances where the torque exceeds the desired value occur to prevent engine misfires and maintain lambda within its limits, and are caused by the need to inject additional fuel due to excess air. Such instances can be observed at large negative torque steps, for example, at time $3900 - 4000$ $[s]$. In Figure 4.19, the boost request compared with the measured boost pressure is plotted together with the ITV valve position during the time periods mentioned above.

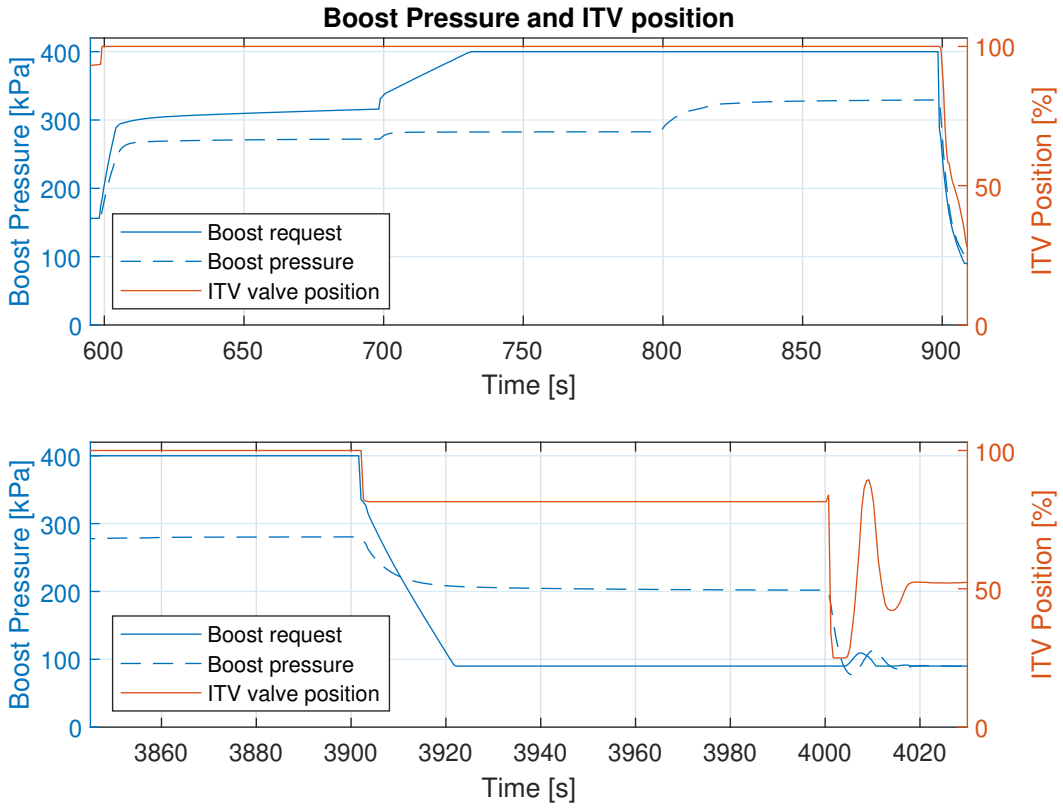

Figure 4.19: Boost request compared to measured boost pressure using lambda control

Figure 4.19 illustrates how the boost pressure cannot build up during low RPMs, even when the ITV valve is fully opened. The ITV valve position results in too high an increase in pressure in large negative torque steps, as it is kept open by the baseline software to protect the engine. The RMSE values of the two strategies for torque tracking are

$$RMSE_{\text{torque},lc} = 0.09 \text{ [Nm]} \qquad RMSE_{\text{torque},r} = 0.03 \text{ [Nm]}. \tag{4.6}$$

4.3.3 Fuel Consumption

In Figure 4.20, the fuel consumption of the lambda control strategy is compared to the consumption of the baseline strategy.

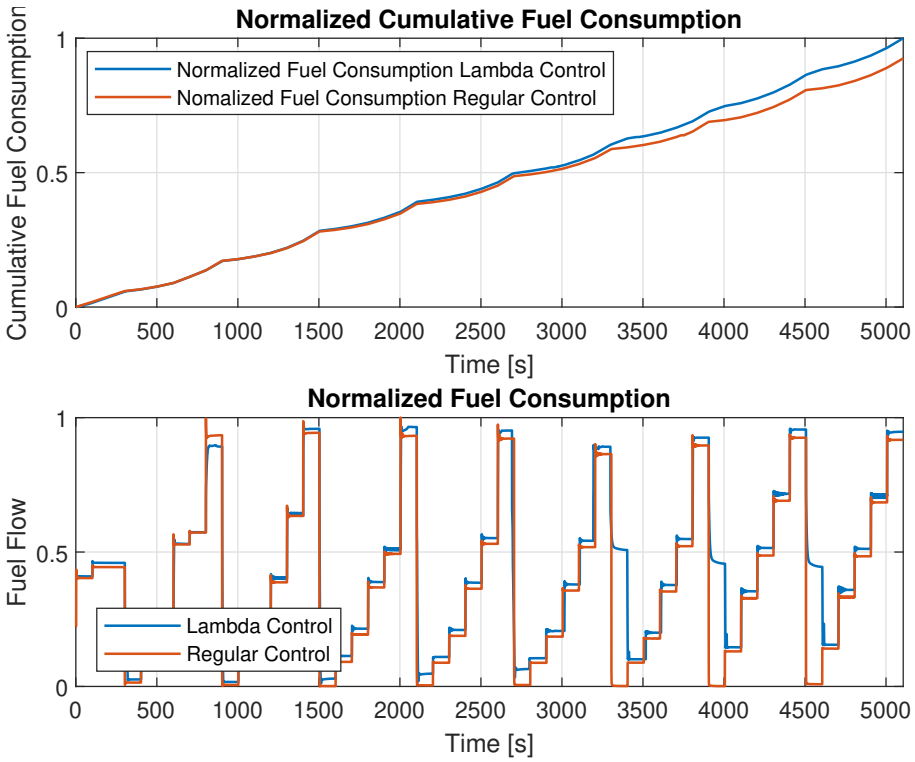

Figure 4.20: Normalized fuel consumption comparison between the lambda control strategy and the baseline strategy

As shown in Figure 4.20, at the early time points, the fuel consumption is very similar for both strategies. During time $730 - 840$ $[s]$, the lambda control strategy consumes less fuel than the baseline strategy due to constrained fuel appertained by engine knocking avoidance. Towards the end, the baseline strategy has distinctively lower fuel consumption. The excess fuel used in the lambda control strategy is due to the additional fuel used for misfire avoidance. The fuel normalized consumption for the two strategies is measured to be

$$m_{fuel,lc} = 1.00 \text{ [kg]} \qquad m_{fuel,r} = 0.92 \text{ [kg]} \tag{4.7}$$

which shows a larger fuel consumption of the lambda controller compared to the baseline strategy.

4.3.4 Performance Without Dead Time Compensation

Upon analysis of the results presented in Section 4.1.1, the difference between the dead time L and the system time constant τ_g was concluded to be minor. This conclusion prompted the analysis of the Otto-Smith dead-time compensator and its impact on controller performance. Lambda tracking was tested with and without a dead-time compensator, and the results are presented in Figure 4.21.

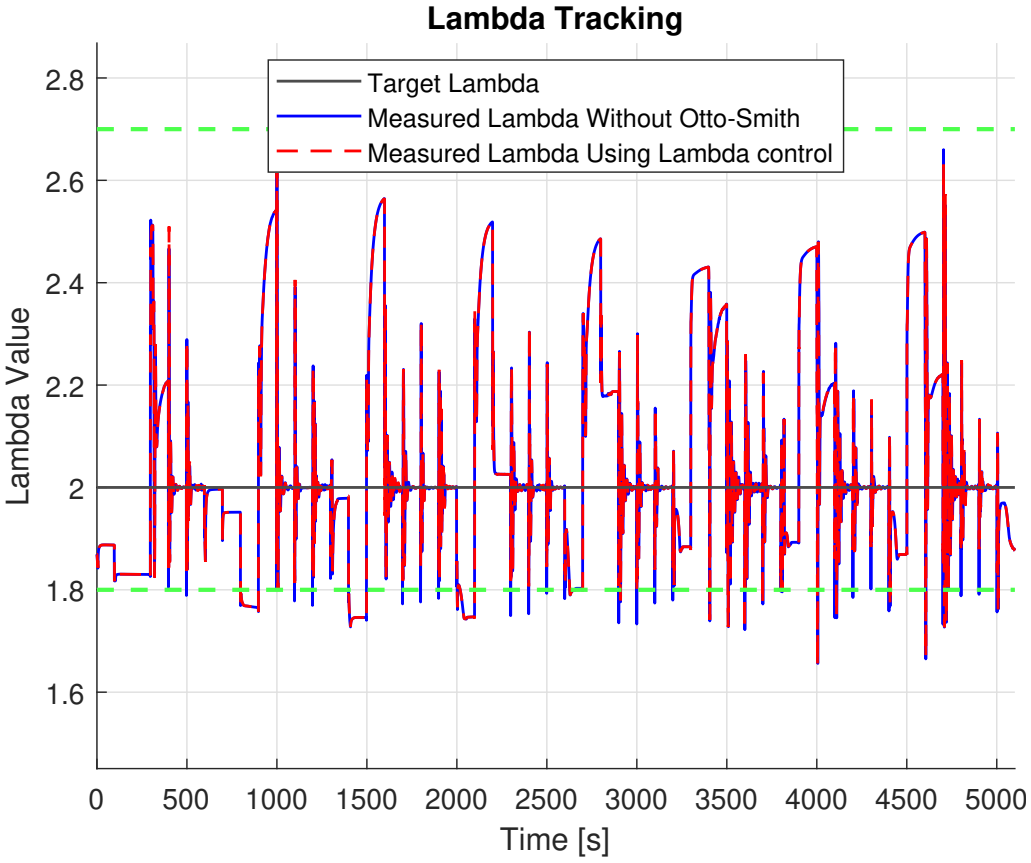

Figure 4.21: Lambda tracking comparison between the lambda control strategy with and without the Otto-Smith compensator enabled

In Figure 4.21, the lambda tracking performance of the two control strategies are observed to be similar. The RMSE values for the lambda control strategy with the Otto-Smith compensator $RMSE_{\lambda,lc}$ and $RMSE_{\lambda,woOS}$ are

$$RMSE_{\lambda,lc} = 0.202 \qquad RMSE_{\lambda,woOS} = 0.203 \tag{4.8}$$

which further established the similarity of the two performances. The constraint violation integral with and without the dead time compensation, CVI_{lc} and CVI_{woOS}, are

$$CVI_{lc} = 26.8\ [\lambda s] \qquad CVI_{woOS} = 27.4\ [\lambda s] \tag{4.9}$$

which signifies a slight decrease in performance for the disabled Otto-Smith compensator. As a consequence, the torque tracking performance metric is nearly identical with and without dead time compensation. Fuel consumption is affected by torque performance, leading to comparable fuel efficiency in both scenarios. See Appendix B for the relevant graphs related to these findings.

To analyze the circumstances where the Otto-Smith predictor proved to improve controller performance, the difference between the errors $e_\lambda = \lambda_{req} - \lambda_{meas}$, i.e $e_{\lambda,lc} - e_{\lambda,woOS}$ was calculated.

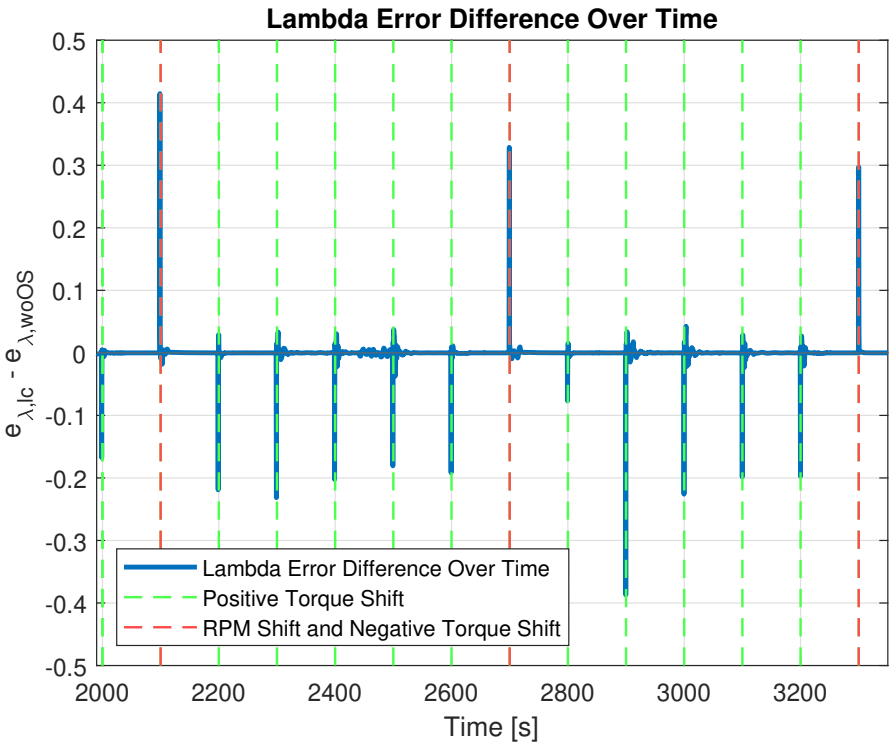

Figure 4.22: The lambda error difference for the lambda control strategy with and without Otto-Smith compensator enabled

The performance is observed to be similar for steady state behavior, evident by the low error values in Figure 4.22. Additionally, the Otto-Smith predictor is shown to perform better in positive transients as opposed to the negative ones.

4.3.5 Performance With EGR

The controller performance is evaluated for enabled EGR, analyzing the effect of EGR on the developed control strategy. Firstly, the ability to track the target lambda is analyzed.

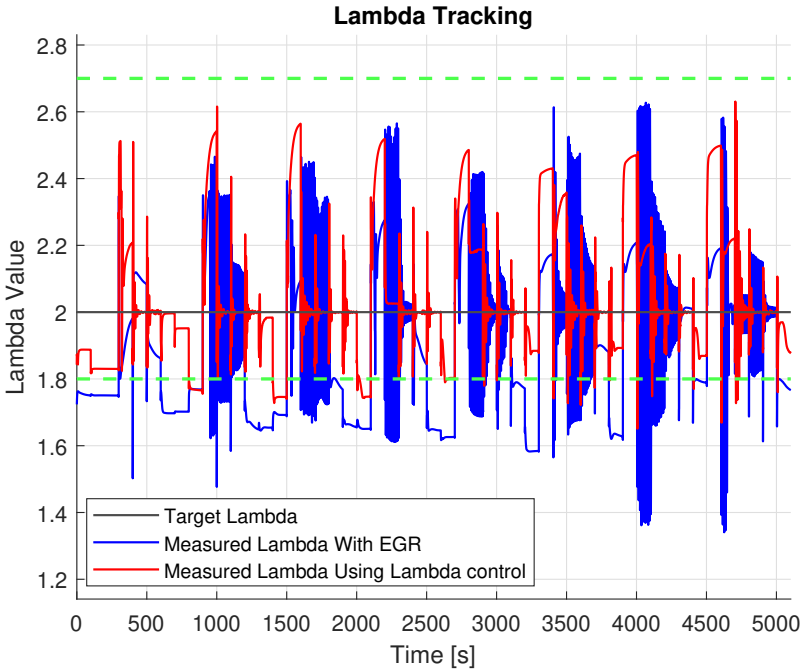

Figure 4.23: Lambda tracking comparison between lambda control strategy with and without EGR enabled

In Figure 4.23, the performance is shown to degrade for enabled EGR with deteriorating stability in multiple instances. The engine performance is also adversely impacted by the enabled EGR. Consequently, the fuel consumption decreases for enabled EGR. See Appendix C for detailed data supporting these observations.

4.4 Chapter Summary

The results show that the air-path lambda controller achieved better lambda tracking than the baseline, but at the cost of increased fuel consumption and slightly worse torque tracking. Using the Otto-Smith compensator made little difference in performance, likely because the system's dead time was relatively small. Enabling EGR led to worse torque tracking and stability. Overall, while the lambda controller met its primary objective of protecting the engine, it came with some trade-offs in terms of drivability and efficiency.

5

Discussion and Future Work

This chapter discusses the results presented in the previous section, evaluating how well the objectives were met. It discusses the estimated system parameters, assesses the effectiveness of the air-path lambda control strategy, and reflects on its impact on engine performance. Finally, it outlines potential improvements and directions for future work based on the findings of this report.

5.1 Discussion of Results

This chapter analyzes the results presented in the preceding one. Also, the evaluation of the problem statement will be presented with concluding answers.

5.1.1 Estimated System Parameters

Analyzing the parameter map for the static gain in Figure 4.1, K is close to 1, which is reasonable because λ_{in} should eventually dissipate to the lambda sensor. Looking at Figure 2.2, two paths exist for the exhaust gases upon entering the exhaust manifold after combustion. One through the VGT compressor and the other through the EGR valve. Regardless of whether the EGR valve is open or closed, the oxygen concentration in the exhaust gases flowing through the VGT compressor to the lambda sensor should remain constant. The static gain should, therefore, theoretically be 1, any deviations from the theoretical value are due to inaccuracies. Inaccuracies can be ascribed to erroneous $\dot{m}_{air}$ and $\dot{m}_{fuel}$ used to calculate λ_{in} or possible defects in the lambda sensor. Such inaccuracies can be observed in Figure 4.4 where λ_{in} is consistently higher than λ_{meas}, regardless of steady-state conditions. The mapped K values are therefore expected to be below 1, as compensation for the aforementioned discrepancies.

Furthermore, the parameter map of the time constant τ_g exhibits behavior that is intuitive to the physical system, as shown in Figure 4.2. Lower RPM and torque values induce slower gas transport dynamics, resulting in larger τ_g. Increasing RPM and torque enables faster gas flow dynamics through the exhaust system, effectively reducing the time constant. Equivalent reasoning can be applied to the dead time L, shown in Figure 4.3, which exhibits the same behavior. One notable aspect of the dead time is that it yields significantly lower values compared to τ_g, especially at higher RPM and loads. These results indicate the irrelevance of a dead time compensator, such as the Otto-Smith predictor.

Conclusively, the intuitive behavior of the model parameters, obtained in Section 4.1.1, asserts confidence in the selected approach. A quantitative indication of the estimated parameter accuracy is the RMSE of the estimated lambda being less than 1% compared to $\bar{\lambda}_{meas}$. Hence, the selected method is proven as a practical approach for parameter estimation of K, τ_g, and L in the process model.

5.1.2 Efficiency of Air-Path Lambda Control Strategy

In Sections 4.3 and 4.2, the implemented air-path lambda control strategy was proven to be effective in controlling the relative AFR. The closed-loop system was verified to be asymptotically stable based on pole-zero analysis and Nyquist diagram evaluation. The lambda control strategy is observed to significantly improve the tracking of the desired λ-values compared to the baseline control strategy, as evidenced by the reduced RMSE and integral error metrics. The RMSE for lambda tracking was reduced from 0.98 to 0.20, and the integral error outside of the acceptable bounds was reduced from 2741 [λs] to 27 [λs]. Acceptable λ-value bounds were maintained during both steady-state and transient conditions. This improvement was expected as the baseline strategy only includes minor considerations for λ-control, such as avoiding soot formation.

Oscillations are present following many transients and are concluded as unrelated to the controller performance. This is due to oscillations at the same time instances for the baseline strategy, observable in Figure 4.17, where the lambda control strategy is disabled. Probable causes for the oscillations are engine construction and various component software, rather than the developed lambda control strategy. Additionally, the lambda control strategy exhibited no oscillations in the simulated step response of the system, as shown in Figure 4.15, which further supports the dissociation between the lambda control strategy and oscillations.

Additional fuel is added as a countermeasure for exceeding the upper lambda limit. However, the controller is observed to add fuel slightly before the lambda limit, which is due to the deviation between the simulated lambda and the lambda measured in test cells, from which the static gain K was determined for this thesis. Consequently, when λ_{in} is calculated according to (3.9), it will differ from the λ_{in}-value measured in the simulation. This explanation can also be applied to observations where λ_{meas} falls beneath the limit.

The Otto-Smith predictor had a negligible impact on the performance because the transport delay of the lambda L was found to be lower than the time constant τ_g, as mentioned in Section 5.1.1. The notable aspect is the performance improvement during positive torque step transients and the performance degradation during negative instances, as observed by the Otto-Smith predictor in Figure 4.22. This aspect may be attributed to the engine test cycle used for the system identification, which did not include large negative transients, resulting in inaccurate parameters during such conditions. Despite a favorable effect during positive torque transient, the per-

formance results were not significantly affected by this aspect due to the test cycle, which primarily consisted of steady-state conditions.

Performance deterioration was observed for the controller during enabled EGR. This is attributed to the disregard of the burned air fraction in the intake manifold, assuming only fresh air in the intake manifold as described in (3.8). Additionally, the parameter maps were determined using data with the EGR disabled. The dynamics for enabled EGR are predicted to differ from the captured dynamics of the system identification, resulting in inaccurate PID tuning fr EGR operation. Lastly, dynamics described in (3.12) may be invalid for enabled EGR due to the flow through the EGR valve. The flow, dependent on the NO_x concentration measured after the VGT, introduces an additional variable to the system.

This concludes the evaluation of the problem statement regarding the effectiveness of using air-path λ-control by stating the efficacy of the solution, achieving AFR targets, and constraining λ to acceptable limits. The Otto-Smith predictor is observed to have a negligible positive impact on the performance of the engine model used in this thesis. Conclusively, the implemented structure of the dead-time compensator and the tuning methodology may benefit future projects with greater transport delay from the engine cylinders and λ-sensor. Lastly, additional work is required for the air-path lambda-controller in systems with EGR, accounting for enabled EGR dynamics.

5.1.3 Lambda Controller Impact on Engine Performance

The lambda control strategy is observed to have higher fuel consumption compared to the baseline strategy, as well as reduced capability to meet the required torque demands. The reduced capabilities are attributed to the fuel limitations imposed to maintain lambda bounds, especially at high torque and low RPM operating points, as shown in Figure 4.18. Additional fuel is added in instances where excessive air supplied by the VGT and the ITV is unable to limit the flow to the intake manifold, as observed in Figure 4.18. The inability of the ITV is due to restrictions imposed by the baseline software, which protects engine components from pressure buildup between the compressor and ITV, as well as vacuum buildup after the ITV.

The majority of operating conditions retain good torque tracking performance with the lambda control strategy. Conclusively, a trade-off exists between torque tracking and fuel economy for multiple operating conditions when using the lambda control strategy, while maintaining similar performance to the baseline strategy for most operating conditions.

5.2 Future Work

This thesis presents the feasibility of using air-path lambda control with some aspects left for further investigation and future improvement. One aspect that warrants further investigation is the modeling and compensation of EGR dynamics, a

necessity highlighted by the degradation of controller performance when EGR is enabled. New feed-forward boost pressure calculations are required, along with the need for updated parameter maps and a revised process model. Modifying (3.8) to account for the burned air fraction $b \in [0, 1]$ in the intake manifold with $\frac{\dot{m}_{air}}{(1-b)}$ as the total air mass flow, resulting in

$$p_{req} = p_i \frac{\dot{m}_{air,req}}{\frac{\dot{m}_{air}}{(1-b)}} = p_i(1-b)\frac{\dot{m}_{air,req}}{\dot{m}_{air}}. \tag{5.1}$$

Although the Otto-Smith predictor proved to be negligible for the setup used during this thesis, it may benefit other engines with larger dead times. Exploring this aspect, by analyzing the Otto-Smith predictor in other engines and conditions, will further develop the evaluation of the potential in using a dead time compensator. There is further benefit in exploring other dead time compensation solutions, such as using a Kalman filter with measured lambda as one state and estimated cylinder lambda as another.

Enhanced speed and precision of control during transients can be achieved with improvements to the boost pressure feed-forward calculations, possibly by modifying (3.8) to account for rapid temperature fluctuations as follows:

$$p_{req} = p_i \frac{T_{in} \cdot \dot{m}_{air,req}}{T_{in,req} \cdot \dot{m}_{air}} \tag{5.2}$$

where $T_{i,req}$ is the intake manifold temperature mapped to the corresponding $\dot{m}_{air,req}$ and the current engine operating conditions. Combining (5.2) with (5.1) gives

$$p_{req} = p_i(1-b)\frac{T_{in} \cdot \dot{m}_{air,req}}{T_{in,req} \cdot \dot{m}_{air}}. \tag{5.3}$$

During this thesis, the control strategy was tested using a simulation environment designed for diesel engines. Testing the lambda controller in either a real H2-ICE or in a simulation environment designed to emulate a H2-ICE is crucial to evaluating the controller's effectiveness in mitigating NO_x emissions.

6
Conclusion

The hydrogen internal combustion engine (H2-ICE) is a promising zero-carbon alternative to conventional diesel engines for heavy-duty applications. However, the properties of hydrogen combustion make air-fuel ratio (AFR) control challenging. Maintaining the relative AFR (λ) within acceptable limits is key to minimizing NO_x emissions and ensuring stable operation. This thesis explores the feasibility of an air-path λ-control strategy to augment AFR regulation.

The estimated parameters were found to represent expected physical behavior accurately and demonstrated high precision. The implemented air-path lambda control strategy proved effective in both tracking lambda and maintaining lambda within the desired bounds. The performance in torque tracking remained relatively similar to the baseline, with some exceptions when the fuel had to be adjusted due to both excess and insufficient air supply. Having an Otto-Smith compensator showed little effect on the accuracy of the controller since the dead time was small relative to the system time constant. Some limitations were noted during EGR operation; however, the controller maintained strong performance and stability overall.

Bibliography

[1] United Nations. *The Paris Agreement*. URL: https://www.un.org/en/climatechange/paris-agreement.

[2] Everett B. Woodruff, Herbert B. Lammers, and Thomas F. Lammers. "Combustion of Fuels". English. In: 10th Edition. Steam Plant Operation. New York: McGraw-Hill Education, 2017. ISBN: 9781259641336. URL: https://www.accessengineeringlibrary.com/content/book/9781259641336/chapter/chapter4.

[3] Volvo Trucks. *Volvo to launch hydrogen-powered trucks*. URL: https://www.volvotrucks.com/en-en/news-stories/press-releases/2024/may/Volvo-to-launch-hydrogen-powered-trucks.html.

[4] European Commission. *European Clean Hydrogen Alliance*. URL: https://single-market-economy.ec.europa.eu/industry/industrial-alliances/european-clean-hydrogen-alliance_en.

[5] Liejin Guo et al. "Hydrogen safety: An obstacle that must be overcome on the road towards future hydrogen economy". In: *International Journal of Hydrogen Energy* 51 (2024), pp. 1055–1078. ISSN: 0360-3199. DOI: https://doi.org/10.1016/j.ijhydene.2023.08.248. URL: https://www.sciencedirect.com/science/article/pii/S0360319923043021.

[6] John B. Heywood. *Internal Combustion Engine Fundamentals*. 1989.

[7] Noveen Alexandra Ng. *DESIGN AND DEVELOPMENT OF ION PROBE TESTING ON FOUR STROKE ENGINE MODEL*. 2016. DOI: 10.13140/RG.2.1.2082.3129.

[8] Jonathan E. Martin. *Global warming*. English. New York, 2023. DOI: 10.1036/1097-8542.291450. URL: https://www.accessscience.com/content/article/a291450.

[9] Sebastian Verhelst and Thomas Wallner. "Hydrogen-fueled internal combustion engines". In: *Progress in Energy and Combustion Science* 35.6 (2009), pp. 490–527. ISSN: 0360-1285. DOI: https://doi.org/10.1016/j.pecs.2009.08.001. URL: https://www.sciencedirect.com/science/article/pii/S0360128509000422.

[10] Cecilia Zambelli. "Exhaust system for hydrogen fuelled combustion engines: effect of high water content on the SCR vanadium catalyst". Master of Science Thesis. KTH Department of Energy Technology, 2020.

[11] Bengt Lennartsson. *Reglerteknikens grunder*. 2000.

[12] Peter Alriksson. *The Otto-Smith Predictor*. URL: https://www.dei.unipd.it/~picci/Files/TEACHING/CONTROLLO_DEI_PROCESSI/SmithPredictor/Presentation_peter_A.pdf.

[13] Torkel Glad and Lennart Ljung. *Control Theory: Multivariable and Nonlinear Methods*. 2000.

[14] Yiming Jiang, Xiaodong Hu, and Sen Wu. "Transformation Matrix for Time Discretization Based on Tustin's Method". In: *Mathematical Problems in Engineering* 2014 (Aug. 2014), pp. 1–9. DOI: 10.1155/2014/905791.

[15] Haiyan Jiang et al. "Comparison of numerical methods and metaheuristic optimization algorithms for estimating parameters for wind energy potential assessment in low wind regions". In: *Renewable and Sustainable Energy Reviews* 69 (2017), pp. 1199–1217. DOI: 10.1016/j.rser.2016.11.241.

[16] E. Lundin. *Adaptive air-fuel ratio control for combustion engines", Master's thesis, Automatic Control, Linköping University*. URL: https://www.diva-portal.org/smash/get/diva2:320940/FULLTEXT01.pdf.

[17] Lennart Ljung. *System Identification: Theory for the User*. 2nd. Englewood Cliffs, NJ: Prentice Hall, 1999. ISBN: 0136566952.

[18] Jorge Nocedal and Stephen J. Wright. *Numerical Optimization*. 2nd. New York: Springer, 2006. ISBN: 0387303030.

[19] Paul T. Boggs and Jon W. Tolle. "Sequential Quadratic Programming". In: *Acta Numerica* 4 (1995), pp. 1–51. DOI: 10.1017/S0962492900002518.

[20] Robert W. Messler Jr. *Engineering Problem-Solving 101: Time-Tested and Timeless Techniques*. 1st Edition. McGraw-Hill Education, 2013. ISBN: 9780071799966. URL: https://www.accessengineeringlibrary.com/content/book/9780071799966/chapter/chapter5.

[21] Xiahai Zhuang and Yipeng Hu. "Chapter 2 - Statistical Deformation Model: Theory and Methods". In: *Statistical Shape and Deformation Analysis*. Ed. by Guoyan Zheng, Shuo Li, and Gabor Székely. Academic Press, 2017, pp. 33–65. ISBN: 978-0-12-810493-4. DOI: https://doi.org/10.1016/B978-0-12-810493-4.00003-1. URL: https://www.sciencedirect.com/science/article/pii/B9780128104934000031.

[22] J. Frausto-Solis et al. "Multiphase Simulated Annealing Based on Boltzmann and Bose-Einstein Distribution Applied to Protein Folding Problem". In: *Advances in Bioinformatics* 2016 (2016). Epub 2016 Jun 20, p. 7357123. DOI: 10.1155/2016/7357123. eprint: https://doi.org/10.1155/2016/7357123.

[23] Esfandiar Shafai, Christian A. Roduner, and H. P. Geering. "On-Line Identification of Time Delay in the Fuel Path of an SI Engine". In: *SAE technical paper series 970613* (1997).

A

Stability Analysis for all Operating Points

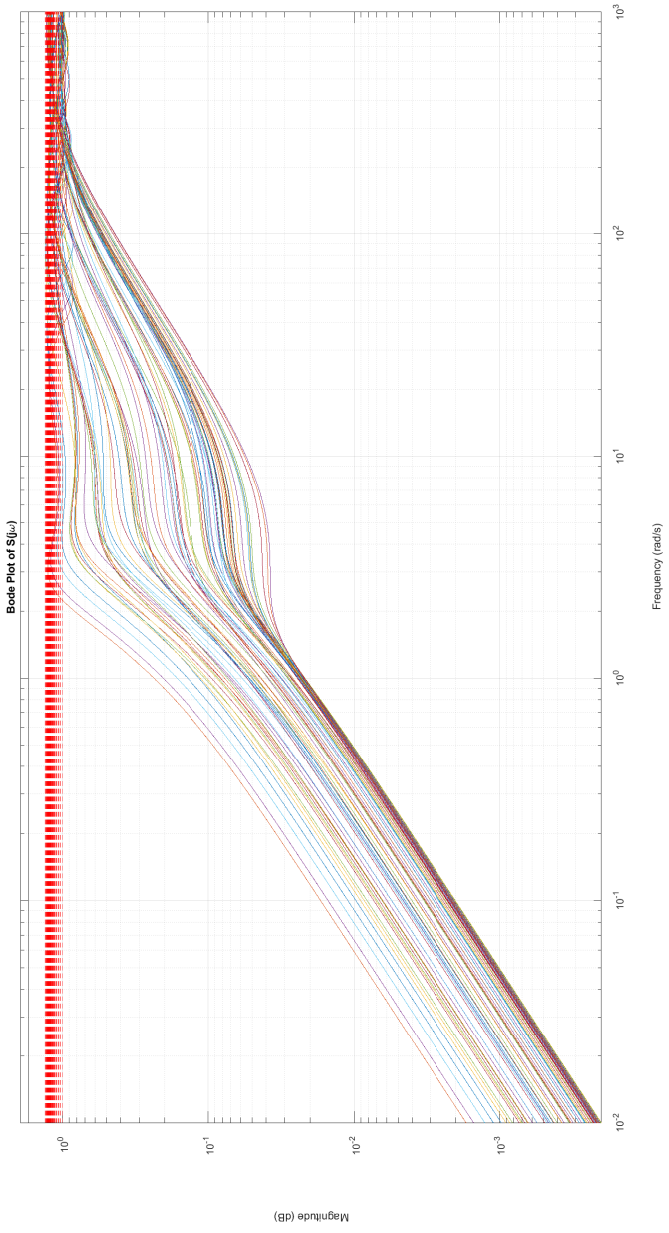

Figure A.1: Bode plot of the sensitivity functions for all operating points

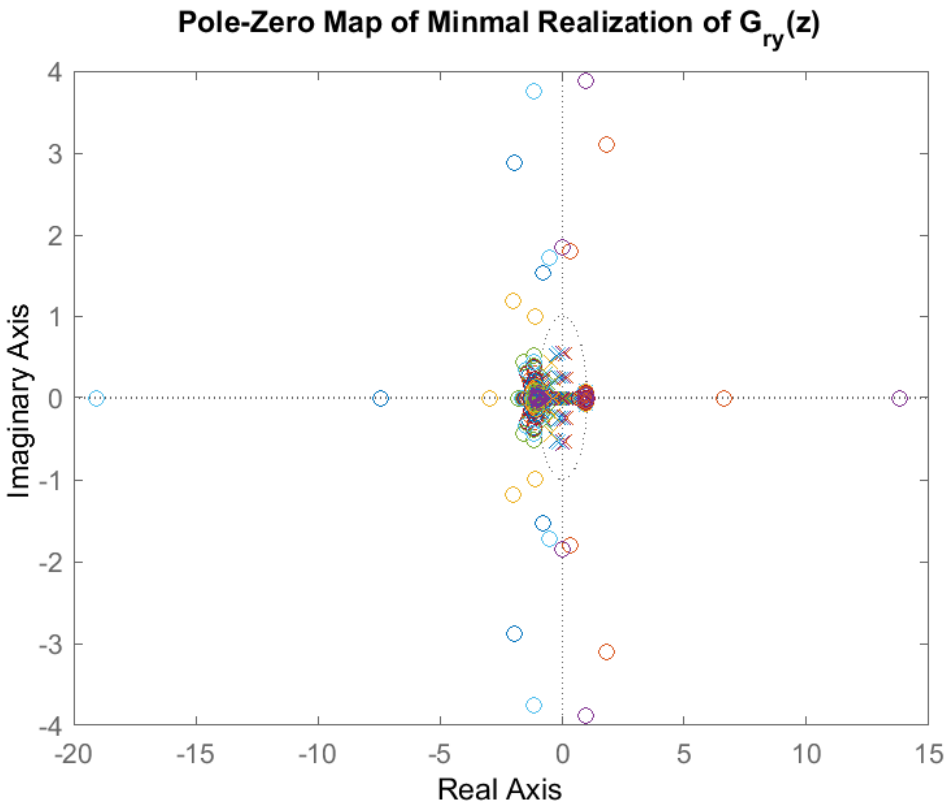

Figure A.2: Poles (marked with ×) and zeros (marked with ∘) of the closed-loop system for all operating points

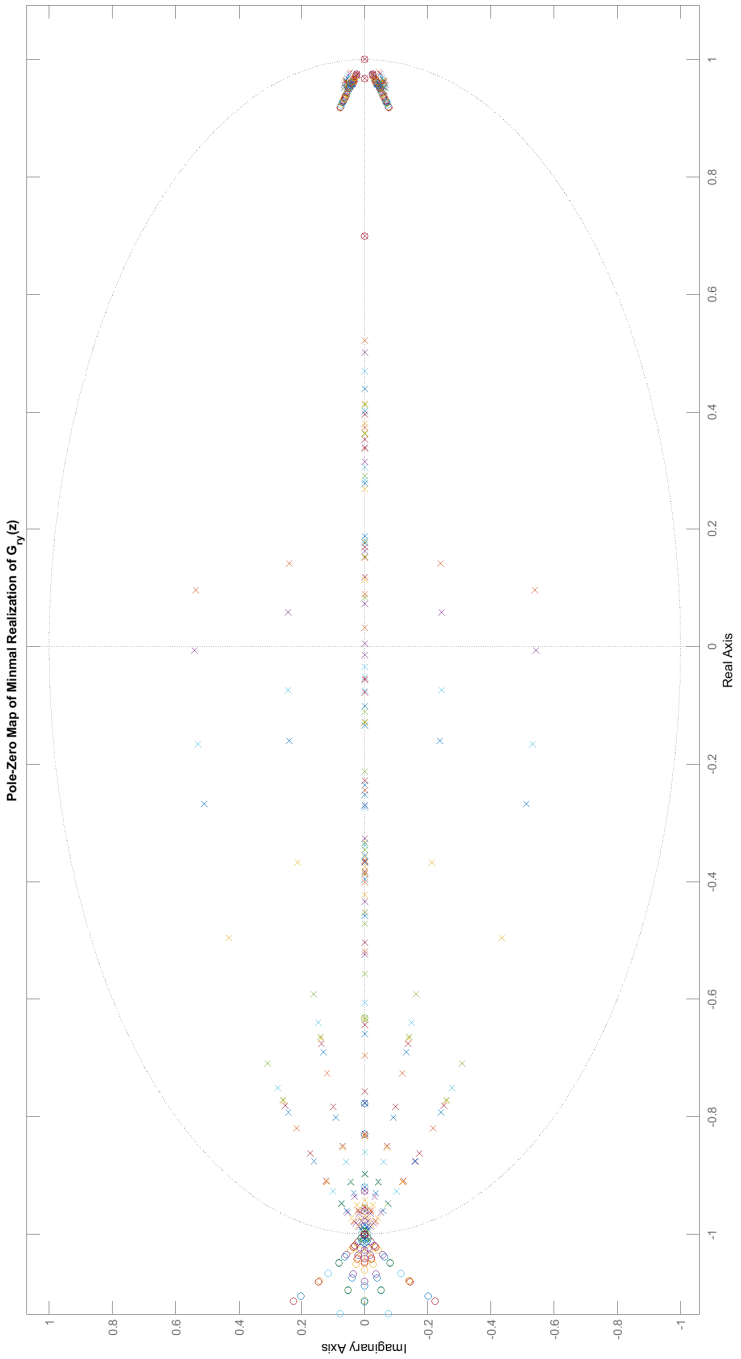

Figure A.3: Poles and zeros of the closed-loop system for all operating points, zoomed in at the unit circle

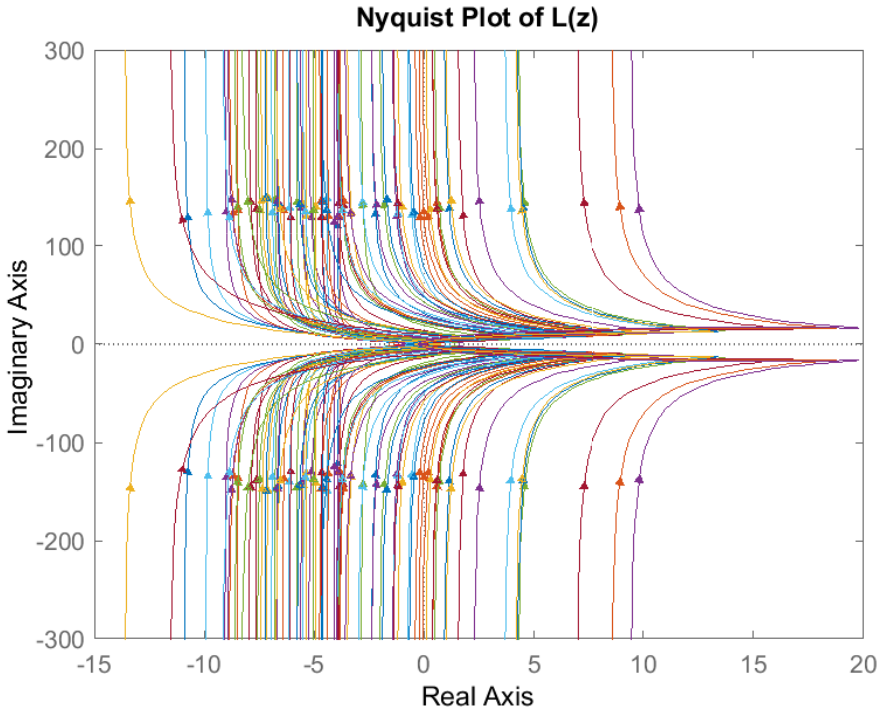

Figure A.4: Nyquist curves of the closed-loop system for all operating points

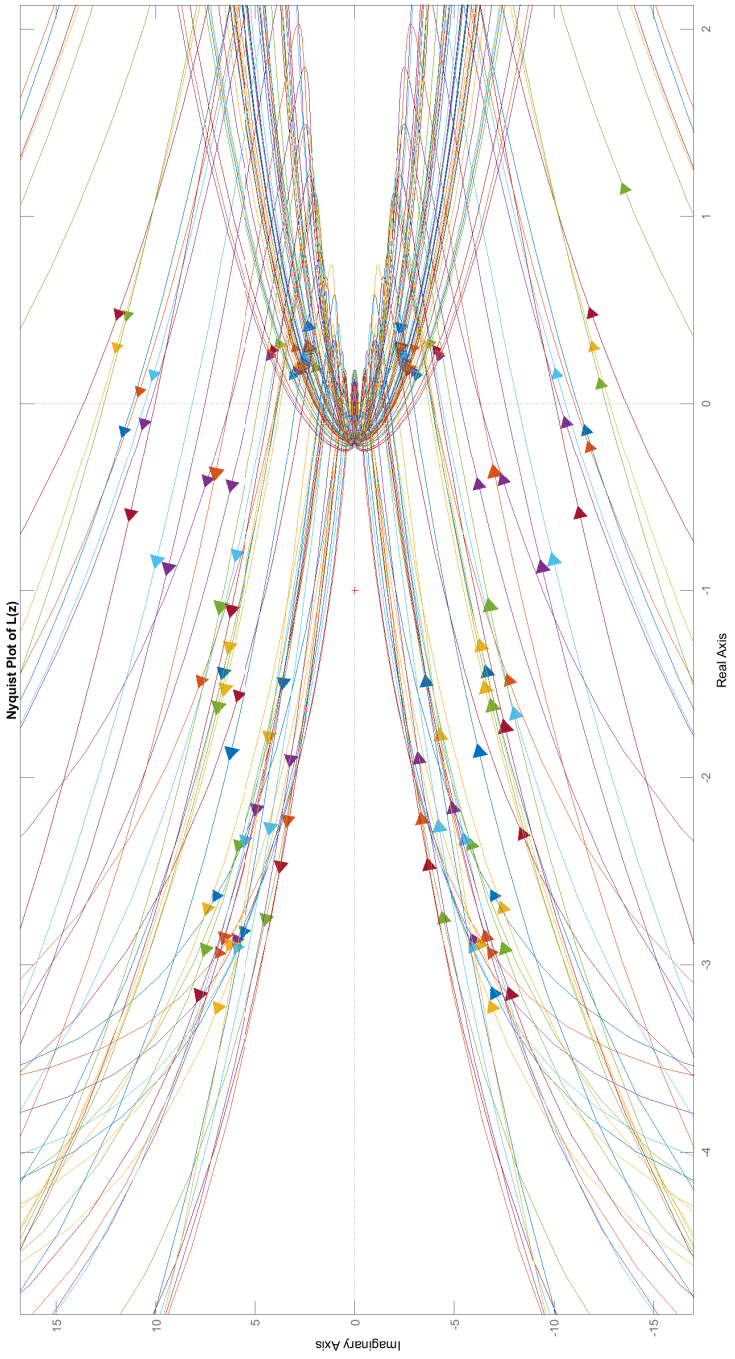

Figure A.5: Nyquist curves of the closed-loop system for all operating points, zoomed in at -1

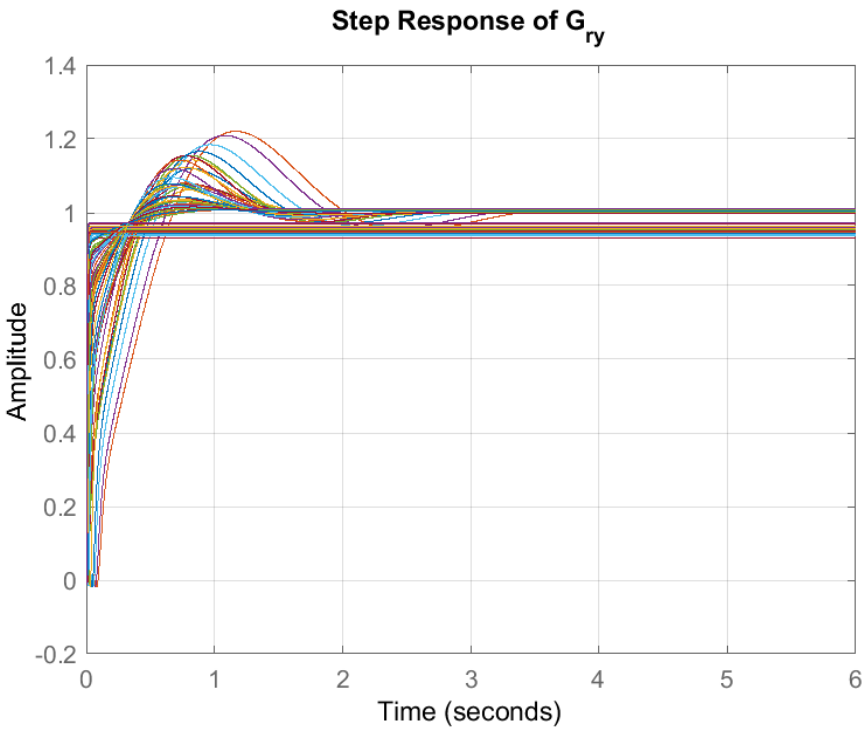

Figure A.6: Step response of the closed-loop system for all operating points

B

Torque Tracking and Fuel Consumption Without Dead-Time Compensation

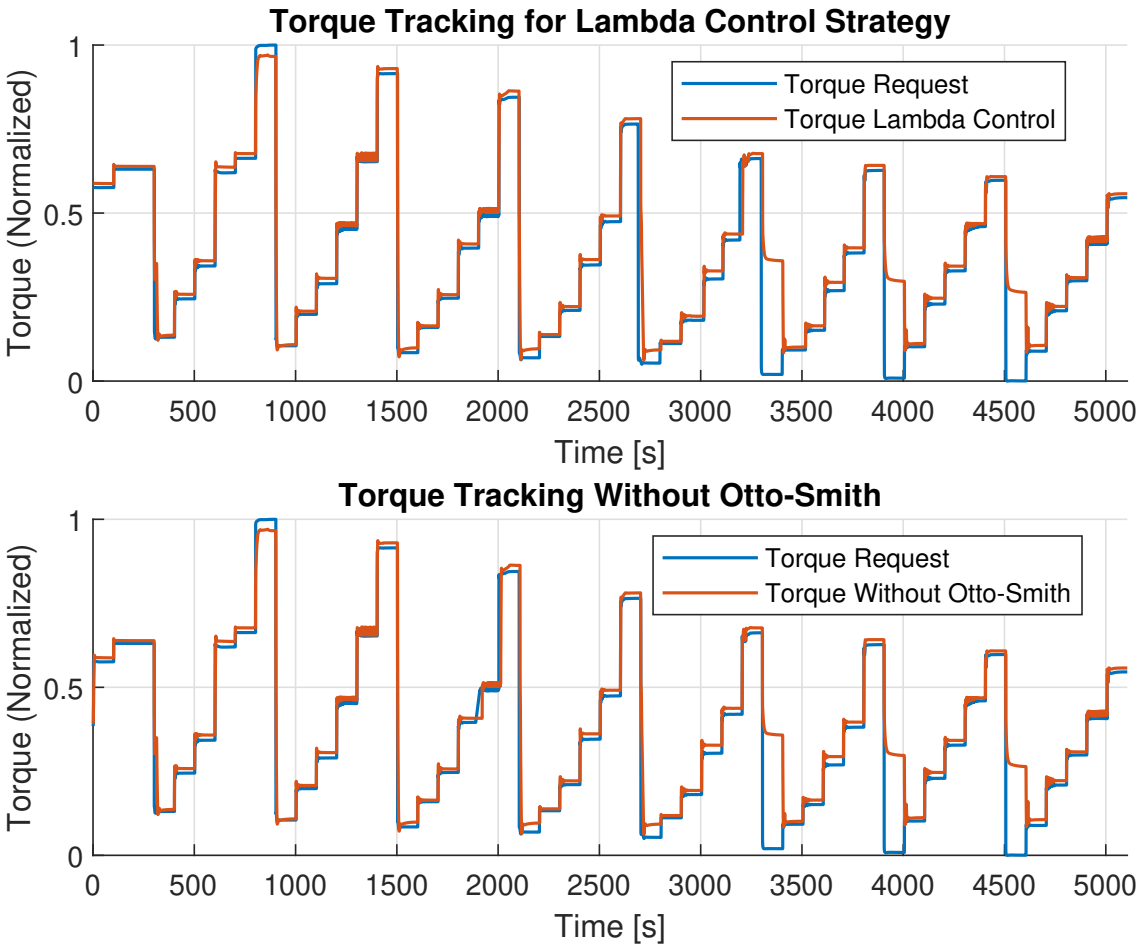

Figure B.1: Torque tracking comparison between lambda control strategy with and without Otto-Smith compensator enabled

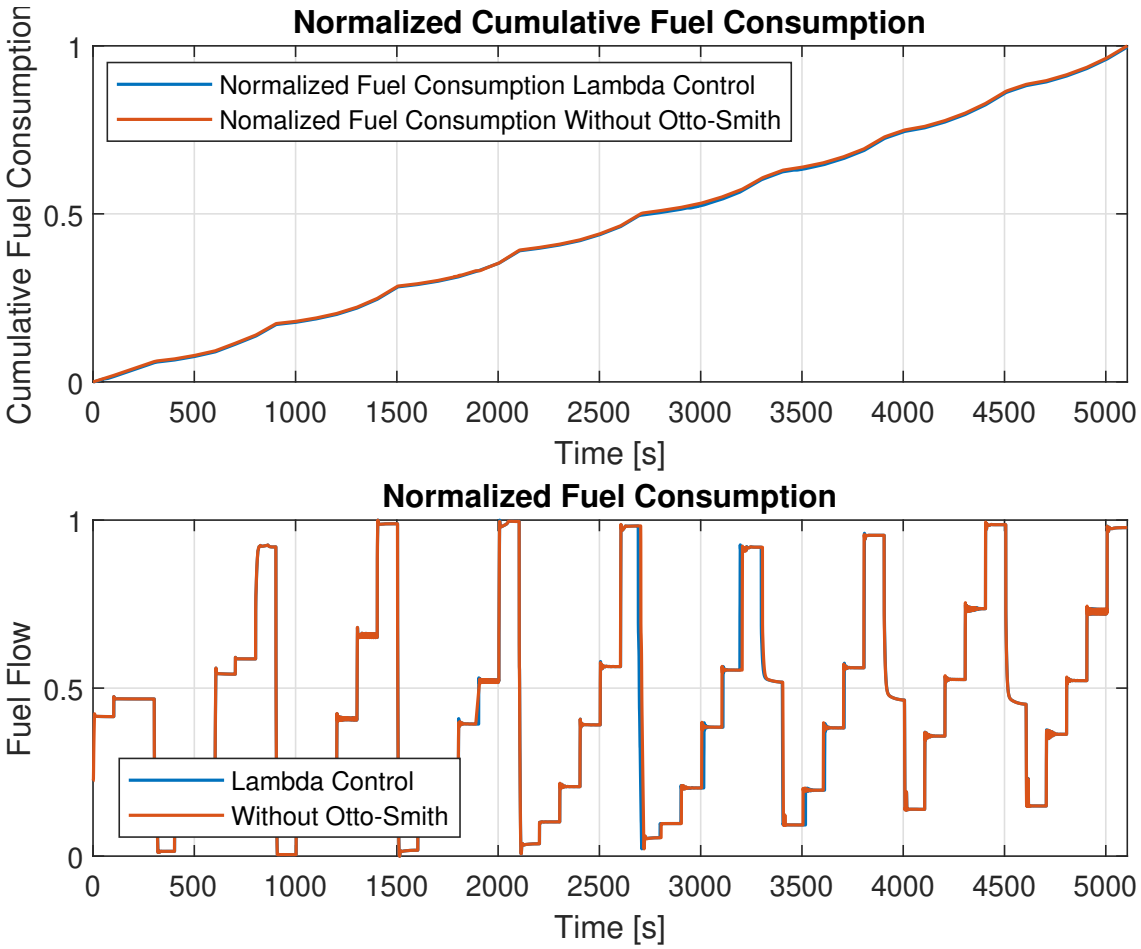

Figure B.2: Fuel consumption comparison between lambda control strategy with and without Otto-Smith compensator enabled

C

Torque Tracking and Fuel Consumption With EGR Enabled

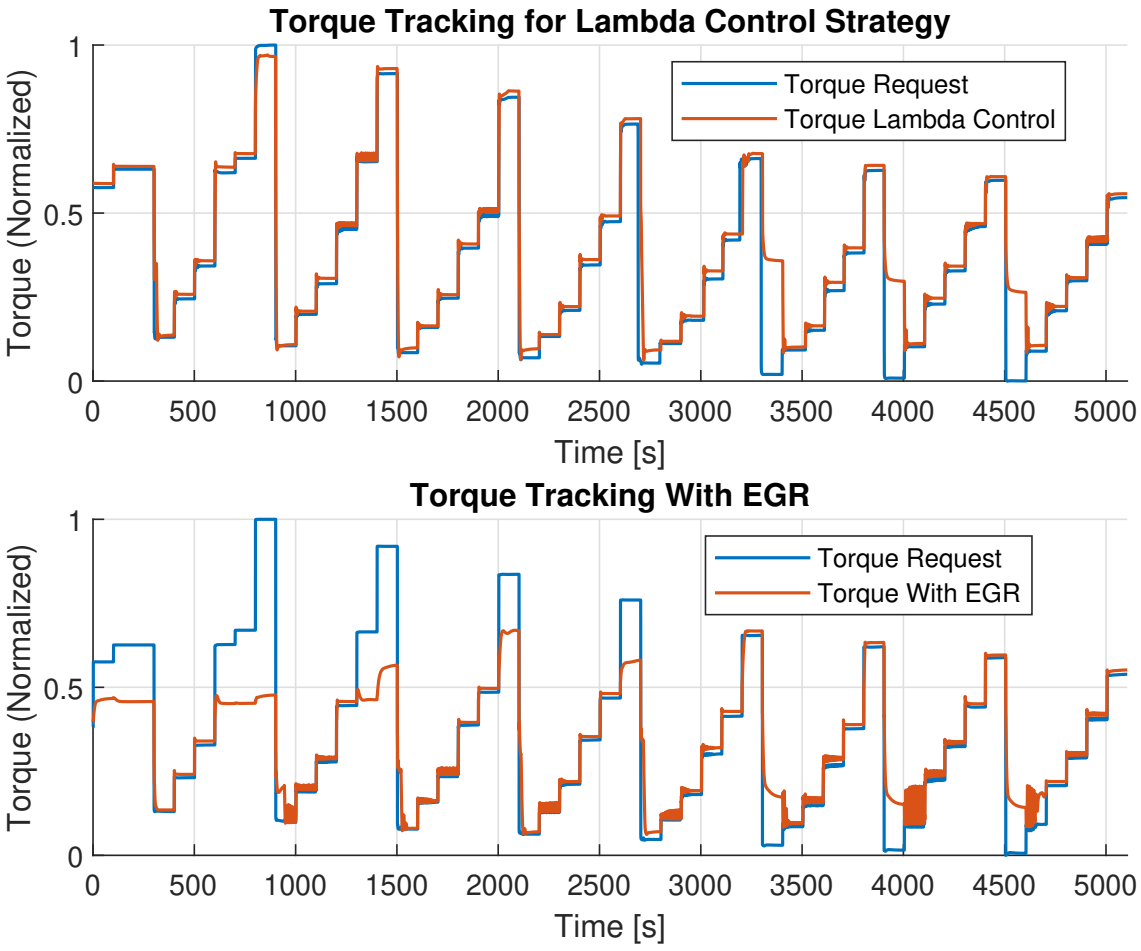

Figure C.1: Torque tracking comparison between lambda control strategy with and without EGR enabled

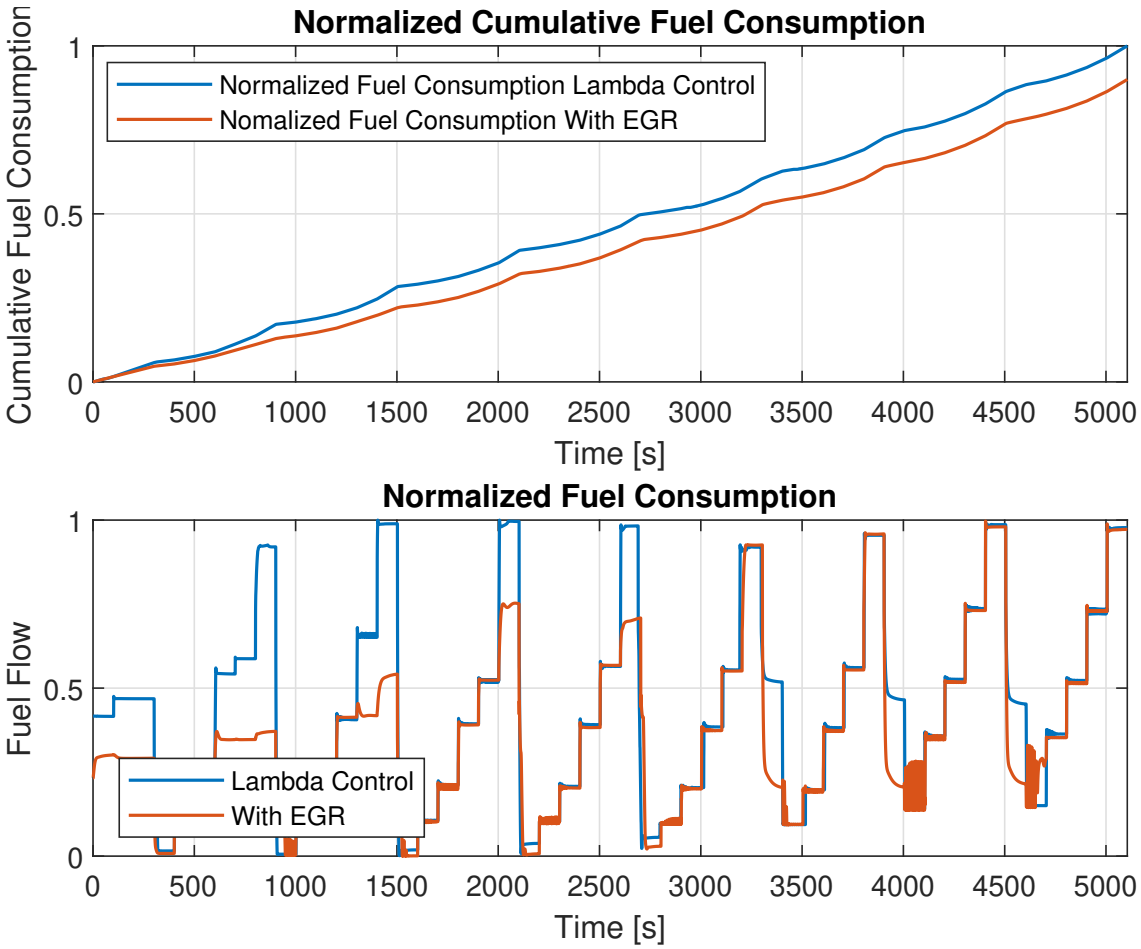

Figure C.2: Fuel consumption comparison between lambda control strategy with and without EGR enabled

DEPARTMENT OF ELECTRICAL ENGINEERING
CHALMERS UNIVERSITY OF TECHNOLOGY
Gothenburg, Sweden
www.chalmers.se

CHALMERS
UNIVERSITY OF TECHNOLOGY